Marine and Petroleum Geology 148 (2023) 106034

Contents lists available at ScienceDirect

Marine and Petroleum Geology

journal homepage: www.elsevier.com/locate/marpetgeo

# A quantitative model and controlling factors of secondary pore development for tight sandstone reservoirs in the carboniferous Benxi Formation, Ordos Basin, China

Jingyi Wang [a,b], Fujie Jiang [a,b,*], Qinhong Hu [c,**], Chunlin Zhang [d], Xiaoguang Yang [e], Wuling Mo [d], Xirong Wang [a,b], Zhenguo Qi [a,b]

[a] State Key Laboratory of Petroleum Resources and Prospecting, China University of Petroleum, Beijing, 102249, China
[b] College of Geoscience, China University of Petroleum, Beijing, 102249, China
[c] Department of Earth and Environmental Sciences, The University of Texas at Arlington, Arlington, TX, 76019, USA
[d] Research Institute of Petroleum Exploration & Development, PetroChina, Langfang, 065007, China
[e] Oil and Gas Survey, China Geological Survey, Beijing, 100083, China

ARTICLE INFO

*Keywords:*
Porosity evolution
Controlling factors
Diagenesis
Tight sandstones
Ordos basin

ABSTRACT

As the Ordos Basin is the largest gas-producing area in China, its central and eastern Paleozoic Carboniferous Benxi Formation is poised to become a significant source for increasing reserves and production within the basin. However, the extreme diagenesis, complex pore structure, and strong heterogeneity of this formation hinder the exploration of its "sweet spots". The reasons are usually considered to be its large burial depth (>3000 m), differential uplift, highly acidic environment and strong hydrocarbon supply in the coal-bearing strata of this area. In this study, we performed qualitative and quantitative analyses of thin sections of Benxi Formation rocks, combined with scanning electron microscopy, X-ray diffraction, and fluid inclusion analyses to determine the development, type, and evolution sequence of secondary porosity from the diagenesis of the Benxi Formation. The main reservoir type of the Benxi Formation is characterized by secondarily dissolved pores (>0.5 μm) and micropores (<0.5 μm) within clay aggregates; the low porosity and permeability of <5.8% and $<1 \times 10^{-3}$ μm$^2$ indicating a tight sandstone reservoir. Throughout the reservoir formation, its porosity has decreased by strong compaction and cementation, and also increased primarily by dissolution. Quantitative analyses of the thin-section porosity of the rocks based on the Scherer initial porosity recovery model and pore evolution parameters defined by Paxton and Ehrenberg showed 39.8% recovery of original porosity and a porosity increase due to dissolution of 1.0–5.4% (mean, 4.1%); this constituted 40–250% of the porosity prior to dissolution. The model-simulated results were closely correlated with the experimental measurements. The lithology, diagenetic fluid, and organic acids of the source rocks jointly controlled the development of secondary pores in the Benxi Formation. These findings indicate that the evolution and controlling factors of secondary pore development must be clarified to identify favorable areas for gas exploration. The results will provide a basis for predicting favorable reservoirs in the tight sandstones of the Benxi Formation in the central and eastern Ordos Basin.

## 1. Introduction

Advances in global energy greening (Oluwadebi et al., 2019) have led to rapid annual growths in proven reserves and production of natural gas (Bai et al., 2021, 2022; Dai et al., 2021; Wang et al., 2021a, 2021b; Yang and Guo, 2021; Zhao et al., 2021). The global proven natural gas reserves reached 188 × $10^{12}$ $m^3$ by the end of 2020 (BP, 2021). Tight sandstone gas has been successfully explored and developed because of its large reserves and extensive worldwide distribution, which includes the East Irish Sea Basin, the Pease Basin in Colorado, the Perth Basin in western Australia, the Western Canada Sedimentary Basin, and the Ordos, Southern Songliao, Sichuan, and Tarim Basins in China (Dai et al., 2021; Nelson, 2009; Oluwadebi et al., 2019; Zou et al., 2019). Tight sandstone gas refers to a gas layer in which the matrix

* Corresponding author. College of Geoscience, China University of Petroleum, Beijing, 102249, China.
** Corresponding author.
*E-mail addresses:* jfjhtb@163.com (F. Jiang), maxhu@uta.edu (Q. Hu).

https://doi.org/10.1016/j.marpetgeo.2022.106034
Received 17 August 2022; Received in revised form 17 November 2022; Accepted 18 November 2022
Available online 24 November 2022

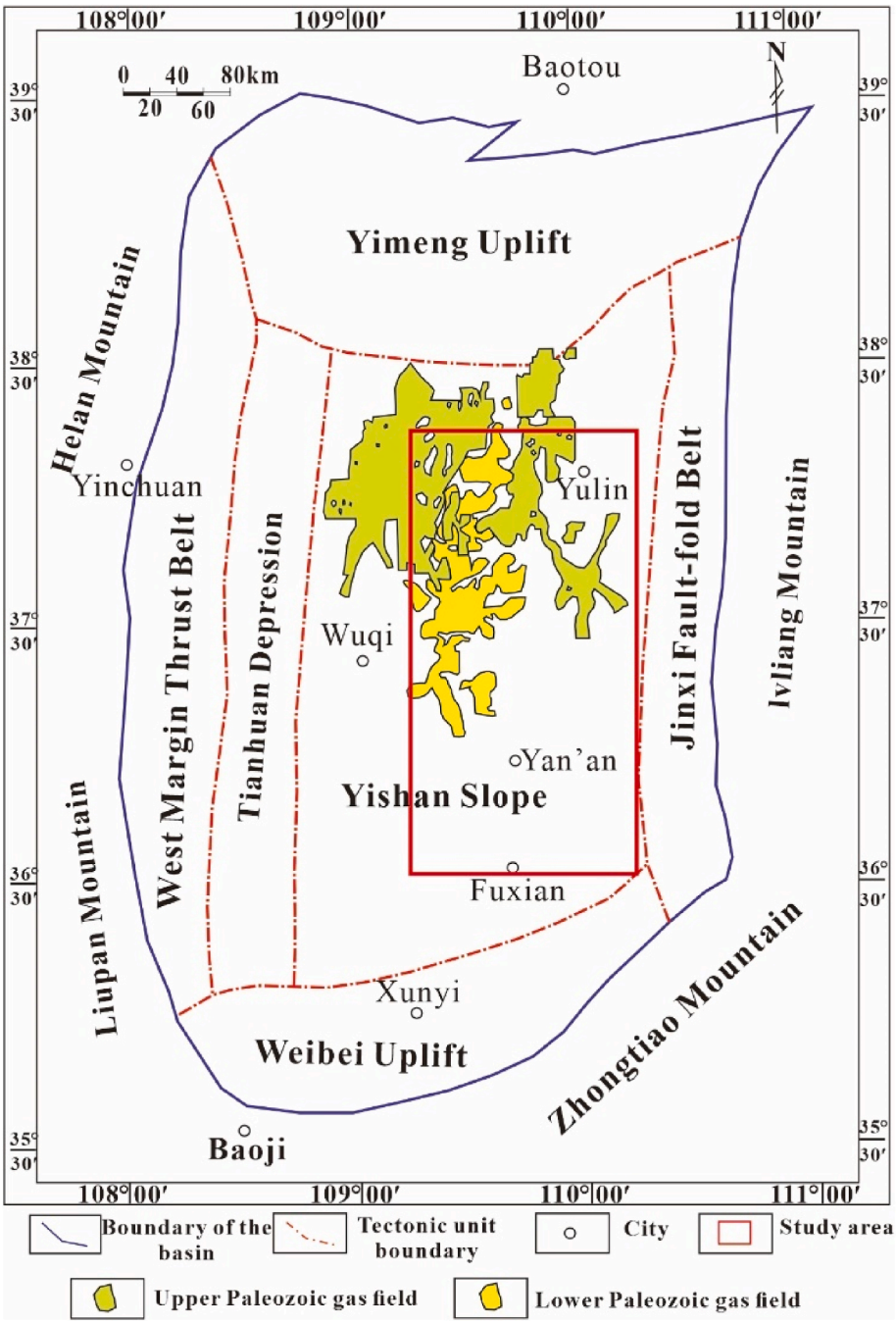


**Fig. 1.** Tectonic map of the Ordos Basin and study area.

permeability is ≤ 0.1 mD (milli-darcy); at such permeability values, single wells generally have no natural production capacity without attaining the lower limit of industrial gas flow, although industrial gas production may proceed under certain economic conditions and technical measures (Zou et al., 2010). China's tight gas production increased from 500 × $10^8$ in 2015 to 800 × $10^8$ $m^3$ in 2020 (Qiu et al., 2011). According to PetroChina's 4th Oil and Gas Resource Evaluation, the total favorable exploration area for tight sandstone gas in China is 32.46 × $10^4$ $km^2$, with total and recoverable resources of 10 × $10^{12}$ $km^3$ and 10 × $10^8$ $km^3$ (Sun et al., 2019; Wang et al., 2021a).

The geological resources of the Ordos Basin are as high as 5.88 × $10^{12}$ $km^3$ in total, comprising >50% of the total geological resources in China, and these resources represent a foundation for the rapid development of tight gas. By the end of 2020, the natural gas of Ordos Basin reached 12.6 × $10^{12}$ $m^3$ (Li et al., 2022), making it the largest petroleum exploration and production base in China. Construction within the Ordos Basin has established the Surig (He 8-Shan 1), Wuzhengqi (He 8), Yulin (Shan 2), Daniudi, Mizhi, and Shenmu (Qian 5) gas fields (Li and Luo, 2005), in which the reserves exceed 1000 × $10^8$ $m^3$ (Wang et al., 2021b; Zhang et al., 2014), mostly from the Shihezi, Shanxi, and Taiyuan Formations (Dai et al., 2021; Li et al., 2021; Wang et al., 2021a).

The Benxi Formation is a deep reservoir that was buried during the Paleozoic, and it has the highest unimpeded flow rate of the Ordos Basin, exceeding 50 × $10^4$ $m^3$/day (Jia et al., 2019a, 2019b; Li et al., 2021). Thus, the Benxi Formation is an important potential replacement area for increasing the future storage and production of oil and gas. Unfortunately, an exploration of the Benxi Formation has been restricted because of its strong heterogeneity and complex pore structure, which

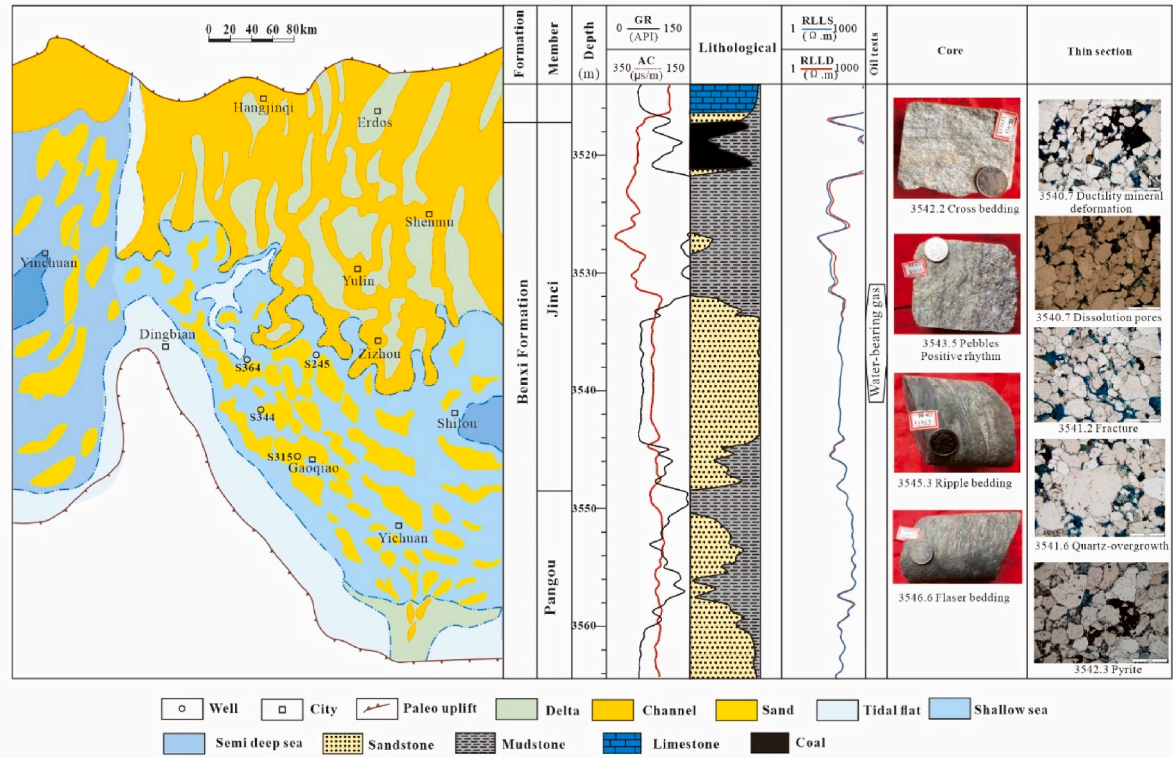


**Fig. 2.** (a) Sedimentary environment of the Ordos Basin; (b) Single-well histogram of the Carboniferous Benxi Formation in the Ordos Basin.

are caused by the complex composition, high clastic content, and strong diagenesis of the formation (Li et al., 2021; Wang et al., 2021b). Dissolution has exposed quartz grain surfaces (Colón et al., 2004; Crundwell, 2014) that connect large numbers of isolated pores and increase the secondary porosity of the rock, which is a key factor that affects the overall porosity and permeability of tight sandstone (Crundwell, 2014; Li et al., 2020; Panagiotopoulou et al., 2007; Pokrovsky et al., 2009). The period-specific dissolved mineral fractions and diagenetic fluid properties also considerably vary in the Benxi Formation. Unstable components within feldspar and rock fragments are most frequently dissolved in acidic environments, and these processes lead to the formation of intra-grain dissolution pores and cast pores generally during the early to middle orogenic stages (Crundwell, 2014; Panagiotopoulou et al., 2007). In contrast, quartz, feldspar, and other silica-aluminate minerals are mainly dissolved during the intermediately late-to-late orogenic stages, which lead to the formation of a port-like shape at the rims of the grains (Crundwell, 2014; Zhong et al., 2007; Panagiotopoulou et al., 2007). The relationship between dissolution and cementation resembles alternating growth and decline of pore development, such that early-stage carbonate cement provides a material basis for dissolution that improves reservoir quality; conversely, clay minerals (e.g., illite, kaolinite, and quartz cement) produced by dissolution remain within the pores of tight sandstone reservoirs, where they can block fluid flow (Zhong et al., 2007; Gier et al., 2008; Hong et al., 2020; Li et al., 2020; Morad et al., 2010; Taylor et al., 2010). As these early-stage tight sandstone reservoirs are located in a highly acidic environment produced by coal-bearing strata in the source rocks (Li et al., 2021; Wang et al., 2021a), which leads to a strong dissolution (Hu et al., 2019a). Thus, to encourage efficient exploration of areas favorable for oil and gas development in the Benxi Formation region, it is important to clarify the sequence of diagenetic evolution, the contribution of various diagenetic processes to increase/decrease porosity, and the factors controlling secondary pore development to predict "sweet spots" within the Benxi Formation.

In this study, we investigated the factors that control secondary pore evolution and the quality of tight sandstone reservoirs in the Carboniferous Benxi Formation of the Ordos Basin using experimental and theoretical studies. The reservoir types, structural characteristics, clastic grain composition, filler and cement composition, and other physical properties of the rocks were extensively studied using thin-section, X-ray diffraction, and scanning electron microscopy (SEM). A quantitative analysis of thin-section porosity (Hu et al., 2019a; Zhang et al., 2014) was based on the Scherer initial porosity recovery (Scherer, 1987) model and pore evolution parameters defined by Paxton and Ehrenberg (Ehrenberg, 1990; Ehrenberg et al., 2009; Paxton et al., 2002), with the original porosity of the rock determined by calculating the decreases and increases in porosity based on the compaction, cementation, and dissolution processes (Beard and Weyl, 1973; Ehrenberg, 1990; Folk, 1957; Paxton et al., 2002; Hu et al., 2019a; Zhang et al., 2014). The objectives of this study were to clarify the sandstone pore evolution pattern during its burial history, delineate the densification process of tight sandstone reservoirs, elucidate the pore evolution and secondary pore development processes based on a tight reservoir pore evolution model that considers both diagenetic and burial processes, and analyze the influences of geological factors (e.g., sedimentary lithology, diagenetic fluids, and hydrocarbon generation) on secondary pore development in the sandstone. The results of this study will provide a basis for predicting favorable reservoirs in the Ordos Basin.

## 2. Geological setting

The Ordos Basin is the second largest sedimentary basin in China, with an area of $25 \times 10^4$ km$^2$ (Jia et al., 2019b; Wang et al., 2021a). Its large interior can be divided into six secondary tectonic belts: Yimeng uplift, Tianhuan depression, western thrust belt, Weibei uplift, Jinxi fold belt, and Yishan slope (Jia et al., 2019a). The study area is located above the Yishan slope, where the formation is a tight sandstone reservoir of Carboniferous System Benxi Formation (Fig. 1).

In the Ordos Basin, the Late Paleozoic stratum includes Carboniferous and Permian; from bottom to top, these are the Benxi, Taiyuan,

Shanxi, Shihezi, and Shiqianfeng Formations (Hu et al., 2019b; Zou et al., 2019). The Benxi Formation was developed through sea-land transition sedimentation after the end of the uplift and denudation of the entire North China Plateau, which corresponded with an increase in sea level. Its reservoir dates to the first set of clastic strata of the North China epeiric sea after the end of carbonate-dominated stratum deposition in the Early Paleozoic, and it was formed in the context of secondary transgression of the North China Craton by the late Caledonian, at approximately 150 Ma (Jia et al., 2019b; Li et al., 2021; Hu et al., 2019a). The period of Ordos Basin formation was characterized by a warm climate and lush vegetation. The depositional environment was influenced by its transformation from marine to terrestrial, with multi-facies superposition of marine, deltaic, and fluvial sand bodies in the longitudinal direction, large contiguous distribution within the plane, and wide development of coal strata. The north portion of the Basin was deltaic, whereas the south was a tidal bar that included a barrier island (Fig. 2a). From bottom to top, the Benxi Formation can be subdivided into the Hutian, Pangou, and Jinci members (Fig. 2b). The Hutian member mainly consists of gray/gray-white bauxite and bauxitic mudstone, deposited as alluvial plain-weathered crustal mudstone or marsh mudstone; the Pangou member consists of dark gray limestone interbedded with gray-white fine to coarse quartz sandstone, limestone, and coal lines; and the Jinci member consists mainly of sandstone, limestone, and coal seams (Wang et al., 2021a, 2021b).

## 3. Experimental methods

### 3.1. Thin-section analyses

Thin-section analyses were performed to determine the grain composition, diagenetic relationships, and pore types of the sandstone (Hu et al., 2019b; Wang et al., 2021a). This work used 56 thin sections collected from 18 wells (M109, M38, M51, M9, Q17, S218, S24, S336, S361, S426, S435, S13, S51, S215, S322, T11, T12, and Y109) in the study area (Fig. 1) for petrographic analyses. All thin sections were vacuum-impregnated with blue epoxy resin to highlight the pores, and 30 of them were semi-stained with alizarin red for carbonate mineral identification using an optical microscope (DMLP, Leica, Wetzlar, Germany). Thus, under the microscopy, a blue color indicated pores, red indicated calcite cement, and purple indicated ferrocalcite cement.

### 3.2. SEM analyses

SEM analyses were performed to characterize the structural relationships among intergranular cement and minerals, clay minerals, and their forms within pores (Hu et al., 2019b; Wang et al., 2021c). This work observed 17 samples collected from seven wells (M109, M51, Q17, S336, S435, T1, and S322) using a Hitachi 4800 SEM (Hitachi Ltd., Tokyo, Japan) at an acceleration voltage of 20 kV. The samples were cut into cylindrical pieces (1 $cm^2$ in diameter, 0.5 cm in height), polished with 200-, 400-, 800-, 1200-, 2000-, and 3000-grain emery paper, dried for 72 h, and coated in gold; they were then examined at magnifications of 30 × to 6000 × .

### 3.3. Porosity and permeability analyses

A total of 17 sandstone samples from nine wells (S247, Y1, S43, M9, S315, M109, S215, Q17, and T12) were tested for their porosity and permeability. All samples were prepared into cylindrical pieces (2.5 cm in diameter, 3 cm in length), cleaned, dried, and placed in a pulse permeameter (PoroPDP-200, Core Laboratories, Amsterdam, Netherlands) for the analyses.

### 3.4. X-ray diffraction analyses

To analyze the mineral composition and clay mineralogy of the Benxi Formation, this research used 32 samples from 16 wells (M109, M38, M5, M, Q1, S24, S31, S33, S39, S42, S43, S5, S21, T1, Y10, and Y16) for whole-rock quantitative analyses and 28 samples from 15 wells (M56, Y1, S5, Y10, M9, M3, T1, Q1, S24, S42, S43, S31, S33, S21, S396) for clay minerals testing. These samples were collected at a depth range of 1950–4000 m. All samples were ground using a 200-mesh ball mill, with each at ≥ 5 g for whole rock and ≥10 g for clays. Samples were measured using an X-ray diffractometer (D/max-2200, Rigaku, Tokyo, Japan).

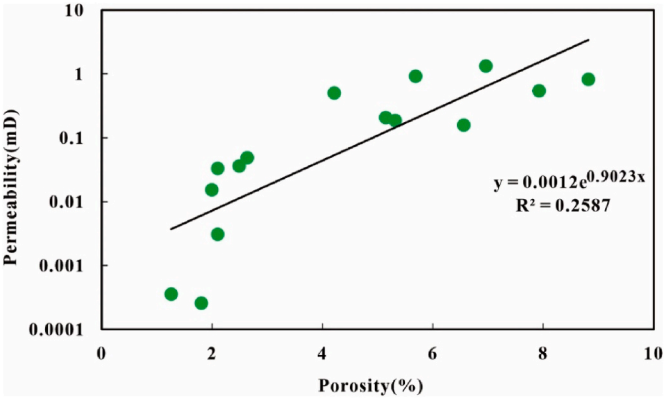


**Fig. 3.** Scatter plot showing porosity and permeability of sandstone in the Benxi Formation.

### 3.5. Fluid inclusions

A total of 30 core samples from 18 wells (M109, M38, M51, M9, Q17, S218, S247, S336, S361, S396, S426, S435, S13, S51, S322, S215, T12, and Y109) in the Upper Paleozoic Carboniferous Benxi Formation in Ordos Basin were selected for fluid inclusion analyses. We used fluorescence irradiation and transmitted light to determine the fluorescence characteristics of hydrocarbon and brine inclusions, respectively. The homogeneous temperature of the fluid inclusions was measured using a THMS 600G hotstage instrument (Linkam Scientific Instruments, Redhill, UK), with a measurement error of ±0.5 °C and a temperature increasing rate of 5 °C/min.

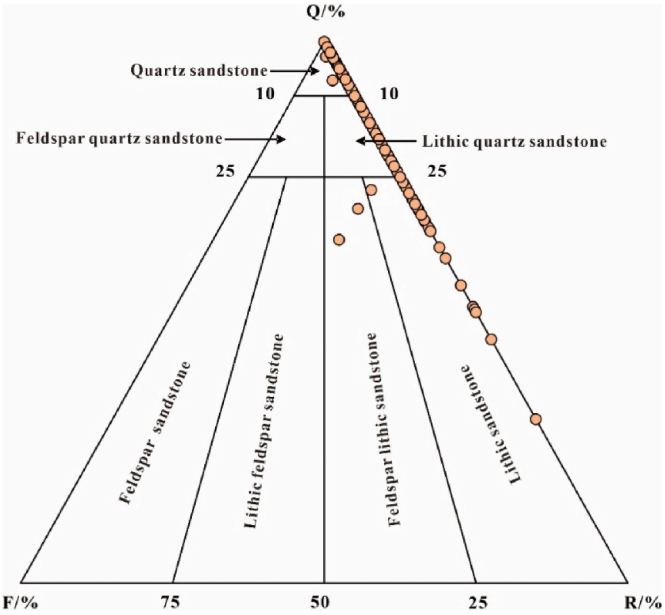


**Fig. 4.** Ternary diagram of Benxi sandstone grain composition; F: feldspar; Q: quartz; R: rock fragments.

**Table 1**
Mineralogy of the Benxi Formation determined by X-ray diffraction.

| Well | Depth (m) | Quartz (%) | K-feldspar (%) | Calcite (%) | Ankerite (%) | Dolomite (%) | Siderite (%) | Gypsum (%) | Pyrite (%) | Clay minerals (%) |
|---|---|---|---|---|---|---|---|---|---|---|
| M56 | 2064.2 | 73.2 | | | 5.5 | | 9.8 | | | 11.5 |
| M51 | 2160.4 | 94.9 | | | | | | | 0.5 | 4.6 |
| Y16 | 2278.9 | 91.5 | | 3.8 | 2.4 | | | | 0.8 | 1.6 |
| Y16 | 2282.9 | 89.0 | | 3.6 | 4.6 | | | | 0.8 | 2 |
| S51 | 2329.3 | 94.1 | | | 0.5 | | | | 0.2 | 5.2 |
| Y109 | 2545.9 | 80.5 | | | 10.1 | | 0.5 | | 0.8 | 8.1 |
| M9 | 2751.6 | 89.4 | | 6.3 | | | | | 0.6 | 3.7 |
| M38 | 2775.9 | 26.6 | | 52.3 | 4.3 | | | | 3.8 | 13 |
| T12 | 2978.1 | 92.2 | | 0.6 | | | | | 1.4 | 5.8 |
| T12 | 2978.6 | 91.8 | | 1.1 | | | | | 0.4 | 6.7 |
| T12 | 2979.8 | 86.1 | | | | | 0.1 | 0.2 | 0.7 | 12.9 |
| T12 | 2985.4 | 86.5 | | 3.1 | | | | 0.1 | 0.4 | 9.8 |
| Q17 | 3025.6 | 94.5 | | | | | | | 0.5 | 5 |
| Q17 | 3027.0 | 74.3 | | | | | 0.3 | | 1.3 | 24 |
| Q17 | 3027.7 | 84.8 | | | | 0.3 | 0.6 | | | 14.4 |
| S247 | 3266.9 | 56.7 | | 39.9 | | | | | 3.1 | 0.3 |
| S247 | 3269.6 | 63.6 | | 5.1 | | | | | 7.9 | 23.5 |
| S247 | 3272.1 | 84.3 | | | 2.9 | | | | 4.2 | 8.6 |
| S426 | 3377.5 | 72.4 | | | 0.2 | | 0.4 | | 0.7 | 26.4 |
| S426 | 3384.3 | 89 | | | 5.9 | | 0.2 | | 0.2 | 4.6 |
| S435 | 3542.3 | 89.4 | | | 2.7 | | 1.9 | | 2 | 3.9 |
| S435 | 3547.3 | 50.1 | 2.7 | | | | 6.8 | | 0.4 | 40 |
| S315 | 3651.0 | 92.2 | | | 4.1 | | 0.7 | | 0.4 | 2.6 |
| S336 | 3829.4 | 91.2 | | | 0.8 | | 0.2 | | 0.9 | 6.9 |
| S336 | 3835.2 | 91.7 | | | 0.6 | | | | 2.6 | 5.1 |
| S336 | 3840.6 | 87.7 | | | 2.7 | | | | 1.5 | 8.1 |
| S215 | 3891.5 | 92.7 | | | 1 | | 1.4 | | 0.5 | 4.5 |
| S396 | 3907.5 | 91.9 | | | 1 | | | | 0.7 | 6.4 |

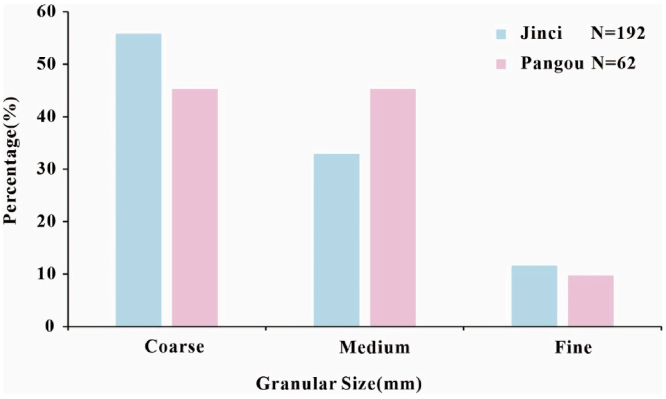


**Fig. 5.** Histogram of sandstone grain size distribution in the Jinci and Pangou Members of Upper Paleozoic Carboniferous Benxi Formation.

## 4. Results

### 4.1. Reservoir porosity and permeability

Porosity and permeability are the two most important reservoir parameters (Jiang et al., 2019; Oluwadebi et al., 2019; Yang et al., 2012). Sandstone in the Benxi Formation consists of tight reservoirs (Wang et al., 2021a) with low porosity and permeability. The porosity ranges from 0.1% to 12.5% (mean, 5.8%), although it is mainly between 2.0% and 8.0%. Samples within porosity intervals of 4–6% and 6–8% are comprised of 30.37% and 31.93% of all samples, respectively. Permeability ranges from $0.003 \times 10^{-3}$ to $1.331 \times 10^{-3}$ μm$^2$ (mean, $0.764 \times 10^{-3}$ μm$^2$), but it is mainly $<1 \times 10^{-3}$ μm$^2$ (Fig. 3). Samples with permeability intervals of $0.01 \times 10^{-3}$ to $0.1 \times 10^{-3}$ μm$^2$ and $0.1 \times 10^{-3}$ to $1 \times 10^{-3}$ μm$^2$ are composed of 26.59% and 53.78% of all samples, respectively. Porosity and permeability were closely correlated in most samples ($R^2 = 0.47$) (Fig. 3).

### 4.2. Petrological characteristics

Thin-section analyses revealed that the main reservoirs of the Carboniferous Benxi Formation are quartz sandstone and lithic quartz sandstone, followed by lithic sandstone (Fig. 4) (Li et al., 2021; Hu et al., 2019a; Wang et al., 2021a). Quartz is predominant among the detrital components, with a monocrystalline quartz content of 86.15% (ranging from 30.27 to 98.84%). The mean lithic rock fragment concentration is 13.72% (0.57–69.73%), and most rock fragments are metamorphic. Thin-section and X-ray diffraction analyses indicated that feldspar content is extremely low (<1.00%) throughout the Benxi Formation (Table 1) (Hu et al., 2019a). The grain size of the sandstone is mainly medium to coarse (Fig. 5), ranging from 0.25 to 1 mm, but it contains small amounts of fine sandstone and granular conglomerate.

The cement content in tight sandstone of the Benxi Formation is generally high, dominated by siliceous, calcareous, and clay minerals (Hu et al., 2019a; Wang et al., 2021a). Kaolinite (3.0–12.0%; with a mean of 7.2%) and illite (3.0–12.0%; 7.2%) are the main clay minerals, whereas chlorite and mixed-layer illite (I/S) are rare (Fig. 6). Other miscellaneous groups represent <10% of the sandstone content.

### 4.3. Diagenesis

#### 4.3.1. Compaction

The burial record showed that the depth of the Benxi Formation is currently >4000 m, whereas it was over 3000 m up to 180 Ma (Hu et al., 2019b). The reservoir was strongly altered by mechanical and/or chemical compaction (Jia et al., 2019b; Li et al., 2021). Most detrital grains show lines of concave-convex contact, even suture lines, under the strong influences of compaction and pressure solution. Thin-section analyses show that detrital grains are in close contact. Feldspar, rock fragment, and ductile grains such as mica have been extruded, resulting in pseudomatrix-like deformation (Fig. 7a and b). Microfractures were generated through the breakdown of brittle minerals, such as quartz. Crystal lattice deformation or dissolution at contact points between minerals was caused by an increasing pressure solution (Yang et al., 2012, 2020a, 2020b; Yuan et al., 2015a,b). Tectonic stress on the rock

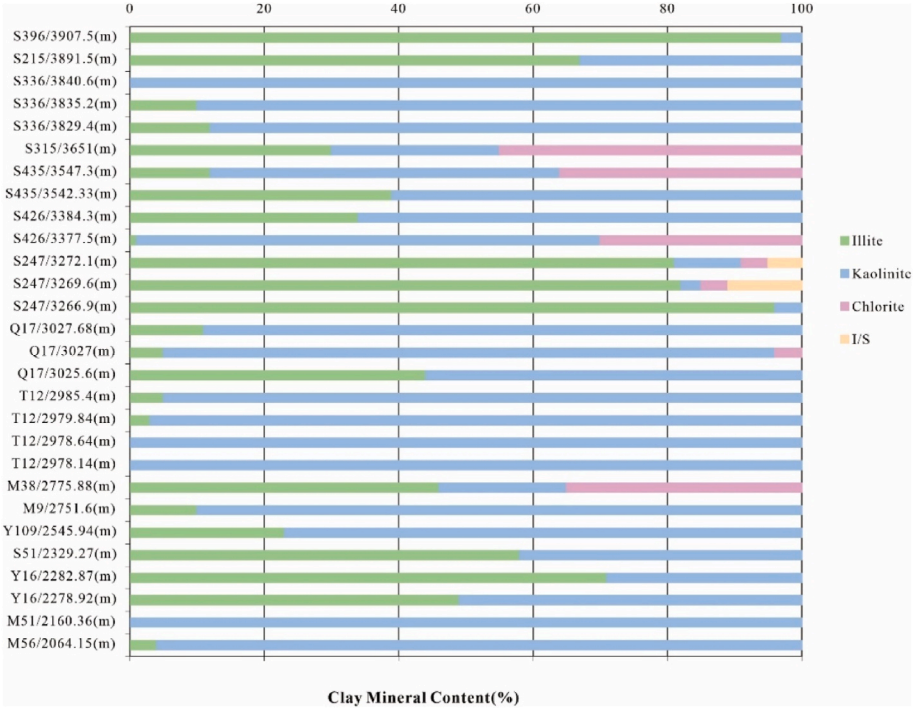


**Fig. 6.** Histogram of clay mineral distribution in the Benxi Formation.

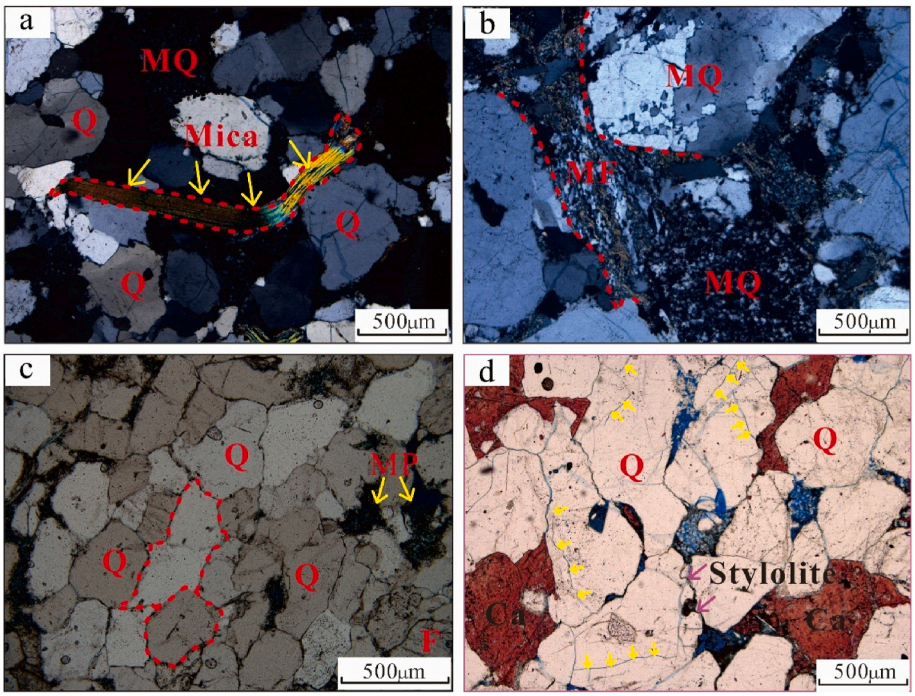


**Fig. 7.** Micrographs showing compaction effects on sandstone in the Benxi Formation; (a–b) Red dashed lines indicate the deformation of (a) ductile grains such as mica and (b) a rock fragment by extrusion for a sample collected at a depth of 3891.5 m in Well S215 (under crossed polarized light, CPL). (c) Red dashed lines indicate concave-convex contact between grains for 3831.0 m in Well S336 (under plain polarized light, PPL). (d) Large numbers of microfractures on quartz grains produced by surface rupture for 2751.6 m in Well M9 (PPL). (For interpretation of the references to color in this figure legend, the reader is referred to the Web version of this article.)

formation seems to consistently exceed the normal fluid pressure within the pore space. Contact relationships between grains were dominated by linear to concave contact (Fig. 7c). Local piezolysis occurs as indicated by suture contacts (Fig. 7d).

*4.3.2. Cementation*

Cementation is a destructive process by which loose sediments harden into sedimentary rock, and it can occur at any stage of diagenesis with an associated reduced porosity (Su et al., 2021; Yang et al., 2020; Zhou et al., 2016). Sandstone in the Benxi Formation underwent various degrees of cementation, as the primary types of cementations involve quartz overgrowths, carbonates, and clay minerals (Li et al., 2021; Hu et al., 2019a). In quartz cementation, authentic quartz fills pore spaces or is attached to the plane of the grains (Fig. 8a, c), and quartz overgrowths occur thereafter. Quartz overgrowths typically occur around grains, resulting in tight reservoirs (Fig. 8b). The hardness of silica enhances the compaction resistance of a reservoir, and this allows some primary pores to persist at the grain rims, while improving the physical properties of tight sandstone reservoirs.

Carbonate cementation is generally attributed to early- or late-stage

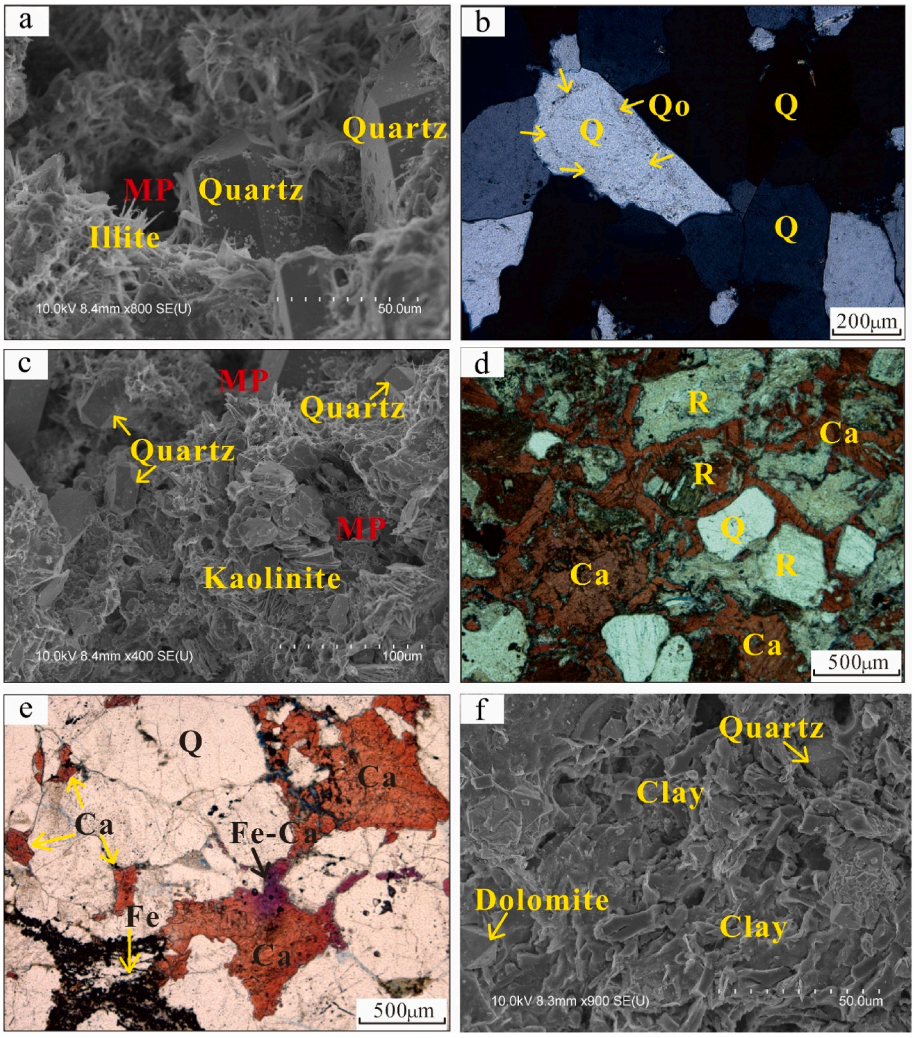


**Fig. 8.** Micrographs of the main cementation types observed in sandstone within the Benxi Formation. (a) Authigenic quartz- and illite-filled pores for a sample collected at 3557.1 m in depth from Well S322 (SEM). (b) Quartz overgrowth close to quartz sandstone grains for 3835.2 m in Well S336 (CPL). (c) Kaolinite clay minerals and quartz filling intergranular pores for 3557.1 m in Well S322 (SEM). (d) Red staining indicates calcite granule-floor cementation, with some grains replaced by calcite for 2775.9 m in Well M38 (PPL). (e) Purple staining indicates late-stage ferrocalcite cementation in the pores for 3720.2 m in Well T11 (PPL). (f) Clay minerals, dolomite, and authigenic quartz coexist in grain pores for 3557.1 m in Well S322 (SEM). (For interpretation of the references to color in this figure legend, the reader is referred to the Web version of this article.)

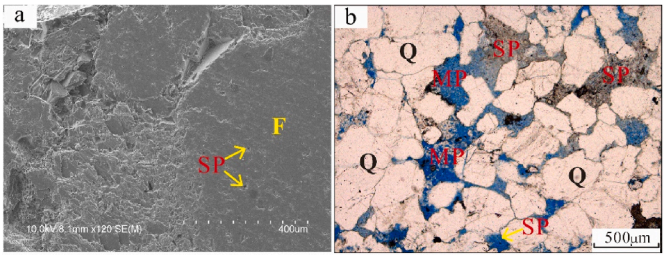


**Fig. 9.** Micrographs of the main dissolution types in sandstone within the Benxi Formation fpr (a) feldspar grains were dissolved to form small craters for a sample collected at 3557.1 m in depth at Well S322 (SEM) and (b) intragranular dissolution pores in rock fragments at 3540.1 m in Well S426 (PPL).

calcite, ferrocalcite, and dolomite (Fig. 8d–f) (Hu et al., 2019a). Early-stage calcite is dissolved by organic acids during early-stage diagenesis. Authentic clay minerals in Benxi Formation reservoirs include kaolinite and illite, along with rare instances of chlorite and mixed illite/smectite. Kaolinite is mainly derived from the dissolution of mineral grains (e.g., feldspar) and rock fragments, and it is also derived from the transformation of heterobase, which manifests as sheet-shape filling in the pores according to microscopic analysis (Fig. 8a, c). Illite is usually fibrous and grows sporadically from attachments to the grain surface (Fig. 8a).

#### 4.3.3. Dissolution

Dissolution is a key diagenetic process that improves the physical properties of tight sandstone reservoirs in the Benxi Formation (Amel et al., 2015; Beard and Weyl, 1973; Zhou et al., 2016). Dissolution can occur in any clastic particles, heterobases, or authigenic clay minerals in the sandstone. In the Benxi Formation, dissolution mainly occurred because of reservoir modification (Hu et al., 2019a) by large amounts of acidic fluids generated during source rock maturation.

Early-stage unstable minerals such as feldspar and rock fragments exhibit harbor-shaped or irregular signs of dissolution, as well as some soluble heterogeneous components and early-stage calcite cementation (Fig. 9a and b). Pores formed by dissolution in the rocks of the study area were mainly contributed by soluble components within the rock fragments because they contain minimal feldspar (Li et al., 2021; Hu et al., 2019a; Wang et al., 2021b).

#### 4.3.4. Metasomatism

Metasomatism is the process by which one mineral is replaced by another (Li et al., 2020; Morad et al., 2010; Nedkvitne et al., 1993; Panagiotopoulou et al., 2007), and it can occur in any stage of diagenesis, including the supergene period. Such replacements are detected in only eight thin sections in this work, highlighting the rarity of metasomatism in the study area (Wang et al., 2021a). Among sandstone in the Benxi Formation, mineral replacement is dominated by calcite cements that replace feldspar, and it was also observed in rock fragments that usually occur along the rims of mineral grains. In these rocks, the outline

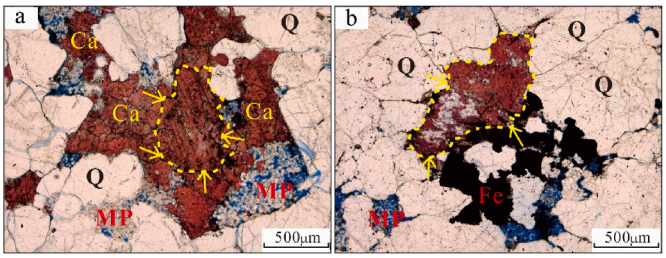


**Fig. 10.** PPL micrographs of metasomatism in sandstone within the Benxi Formation for (a) calcite replacing orthoclase in a sample of 2751.6 m in depth from Well M9 and (b) feldspar particles replaced by calcite after dissolution for 2978.1 m a sample collected in Well T12.

and morphology of the primary grains are preserved, but the composition has changed (Fig. 10a and b).

### 4.4. Fluid inclusions

Microscopy analyses showed that fluid inclusions in sandstone within the Benxi Formation are mainly developed within the microfractures of quartz grains (Fig. 11a) (Hu et al., 2019a), with some development in quartz overgrowths (Fig. 11b). The compositions of these fluids include $CH_4$, $N_2$, and $CO_2$, among which $CH_4$ is dominant. There are two main types of reservoir fluid inclusions in the study area: brine inclusions and brine inclusions containing gaseous hydrocarbons (Hu et al., 2019b).

Brine inclusions are colorless and transparent under polarized light microscopy without emitting light under fluorescence, and they are distributed individually or in a manner similar to strung beads. Brine inclusions are often observed in quartz microfractures, with small amounts produced in quartz overgrowths. Their sizes mainly vary from 2 to 8 μm, and their shapes can be round, elongated, or irregular, with a clear outline. The amount of brine inclusions containing gaseous hydrocarbons in the sandstone of the Benxi Formation reservoir is considerable. These inclusions mainly appear as circular, ellipsoid, or long beads strung along fractures; in addition, they are generally 4–7 μm in size, although occasionally reaching 15 μm. These inclusions are colorless or light-brown under plane-polarized light (Fig. 11c, e) and blue under fluorescence (Fig. 11d, f).

The formation of oil and gas reservoirs can be dated according to the homogenization temperature of brine inclusions (Li et al., 2021; Hu et al., 2019a), combined with the burial history and geothermal evolution history of the strata where the inclusions are located (Hu et al., 2019b). A plot of 120 homogenization temperature measurements shows that the homogenization temperatures of brine inclusions in the Benxi Formation range from 82 °C to 168 °C (mean, 140 °C), with two main peaks at 100–110 °C (24 inclusions) and 130–135 °C (40 inclusions) (Fig. 12). These findings are indicative of two hydrocarbon formation events in the Upper Paleozoic Carboniferous Benxi Formation of Ordos Basin, as also being reported by Wang et al. (2021b).

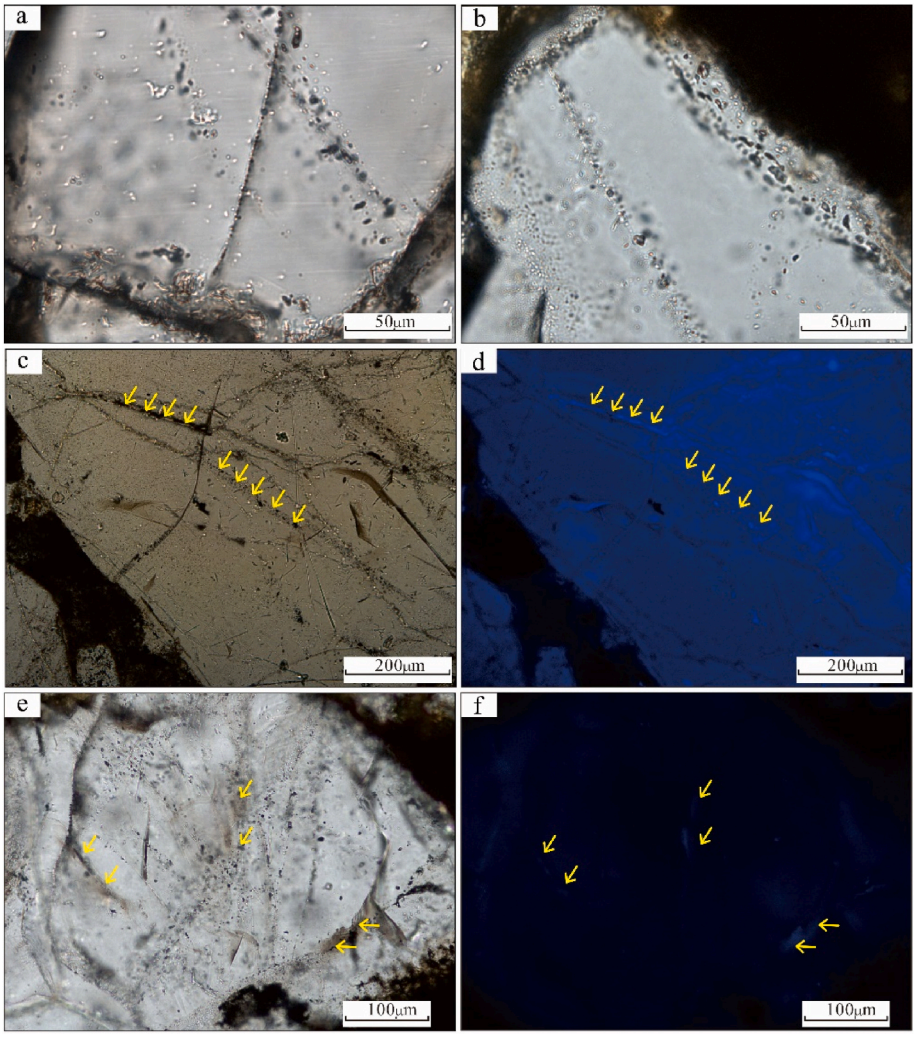


**Fig. 11.** Micrographs of fluid inclusions in sandstone within the Benxi Formation; (a) Brine inclusions resembling strung beads observed in quartz microfractures for a sample collected at 3892.0 m in depth in Well S361 (PPL). (b) Brine inclusions produced in quartz overgrowths at 2545.9 m in Well Y109 (PPL). (c–d) Brine inclusions containing gaseous hydrocarbons observed in quartz microfractures under (c) PPL and (d) UVL for a sample collected at 3891.5 m in depth in Well S215. (e–f) Brine inclusions containing gaseous hydrocarbons observed in microfractures and quartz overgrowth under (e) PPL and (f) UVL for a sample at depth of 2545.9 m in Well Y109. UVL, ultraviolet light.

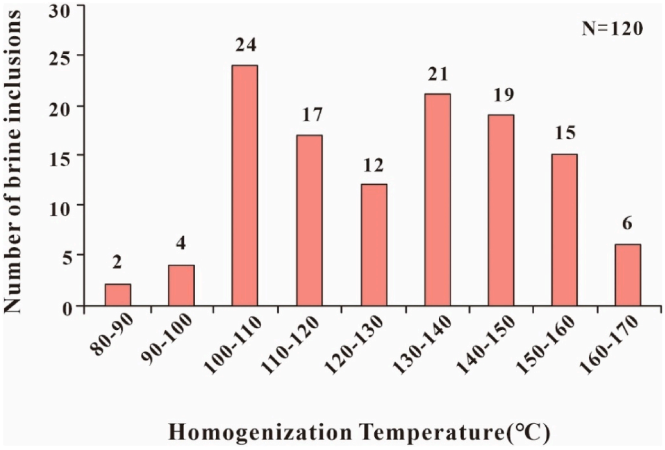


**Fig. 12.** Homogenization temperature histogram for the Benxi Formation.

### 4.5. Diagenetic stages

The reservoir burial depth of the Benxi Formation is currently 2000–4000 m, but it has been >4000 m in the past (Hu et al., 2019a; Wang et al., 2021a). It has been reported that the vitrinite reflectance Ro in the study area ranged from 1.8% to 4.0% (Li et al., 2021), with high organic matter maturity, and the maximum temperature ranged from 539 °C to 568 °C (Hu et al., 2019a). The homogeneous temperatures of fluid inclusions for 120 samples range from 82 °C to 168 °C (mean, 140 °C) (Fig. 12). Based on the combined results of thin-section analyses and SEM observations, we conclude that the Benxi Formation is mainly in the Mesodiagenesis B stage, and partly in Telodiagenesis (Fig. 13), with the following five stages of diagenetic evolution being experienced according to the literature.

**Eodiagenesis A**: In this stage, the burial depth of the strata was approximately 500 m, with a paleotemperature of <65 °C. The organic matter was immature (Ro < 0.35%). The rocks were weakly to semi-consolidated, and the primary pores were developed. Illite and montmorillonite formed a disordered mixed layer. Large amounts of microscopic authigenic kaolinite cements were present because anorthite is easily dissolved at low temperatures (Hu et al., 2019a-b; Yuan et al., 2015a,b). The hydration of minerals (e.g., mica) at this stage led to and increasing alkalinity and production of $Mg^{2+}$ & $Fe^{2+}$. Compaction was the action with the greatest influence on pore space in this stage, and it caused rapid reduction in porosity and water discharge, with grains forming point to linear contacts. Simultaneously, unstable rigid grains experienced a slippage, which resulted in tight and solid grains.

**Eodiagenesis B**: At this stage, the stratigraphic burial depth was between 1500 and 2000 m, with a paleotemperature of 65–85 °C. The organic matter was immature (Ro = 0.35–0.50%) (Hu et al., 2019a). The rock transitioned from semi-solid to consolidated, in a manner influenced by the compaction and cementation. The reservoir remained dominated by primary pores, with small numbers of secondary pores and a mixed layer of disorderly illite and montmorillonite clay minerals. Class I quartz overgrowths were interlaced with commonly authigenic kaolinite in book-like patterns, and calcite cements began to replace mineral grains. Feldspar was partially dissolved in the acidic diagenetic environment caused by organic acid production from coal-bearing strata. K-feldspar was altered to form authigenic kaolinite because of the lack of support stratigraphy, which allowed the dissolution of early carbonate cement and the easy compaction of minerals and grains.

**Mesodiagenesis A**: At this stage, the stratigraphic depth was generally 3000 m (>3500 m in some areas), with a paleotemperature of 85–140 °C. The organic matter was immature (Ro = 0.5–1.3%) (Hu et al., 2019a). The illite/smectite mixed layer was partly ordered (15–35%). Coal-bearing strata produced organic acids, which dissolved large quantities of feldspar; in addition, the resulting release of $Ca^{2+}$ led to the emergence of late-stage carbonate cements, including ferrocalcite and ankerite. Class II quartz overgrowths and authigenic quartz began to appear, and clay minerals including kaolinite and illite were produced in large quantities. Dissolution pores were formed in large quantities because of high organic acid production.

**Mesodiagenesis B**: At this stage, the burial depth of the entire Benxi Formation was >4000 m, with a paleotemperature of 140–175 °C. Organic matter was very mature (Ro = 1.3–2.0%) (Hu et al., 2019a). Class III overgrowths were found in a few thin sections from the south part of the formation, with mosaic-like contacts. The presence of kaolinite minerals substantially decreased and the illite/smectite mixed layer continued to transform into illite and chlorite, forming ferrocalcite cements. Large amounts of calcareous cement led to dense rock formation when they were unaffected by dissolution. Microfractures were also developed in reservoirs with high brittle mineral content, as well as areas of stress and strain.

| Diagenetic stage | Eodiagenesis | | Mesodiagenesis | | Telodiagenesis |
|---|---|---|---|---|---|
| | A | B | A | B | |
| Depth(m) | 500 | 1500~2000 | 3000 | 4000 | >4000 |
| Paleogeotemperature (℃) | <65 | 65~85 | 85~140 | 140~175 | 175~200 |
| Ro(%) | <0.35 | 0.35~0.5 | 0.5~1.3 | 1.3~2 | >2 |
| Tmax(℃) | <430 | 430~435 | 435~460 | 460~490 | >490 |
| Compaction | | | | | |
| Quartz overgrowth | | | | | |
| Carbonate cementation | | | | | |
| Kaolinite | | | | | |
| I/S | | | | | |
| Illite | | | | | |
| Chlorite | | | | | |
| Dissolution | | | | | |
| Fluid environment | | | | | |



**Fig. 13.** Evolutionary sequence of reservoir diagenesis in the Benxi Formation.

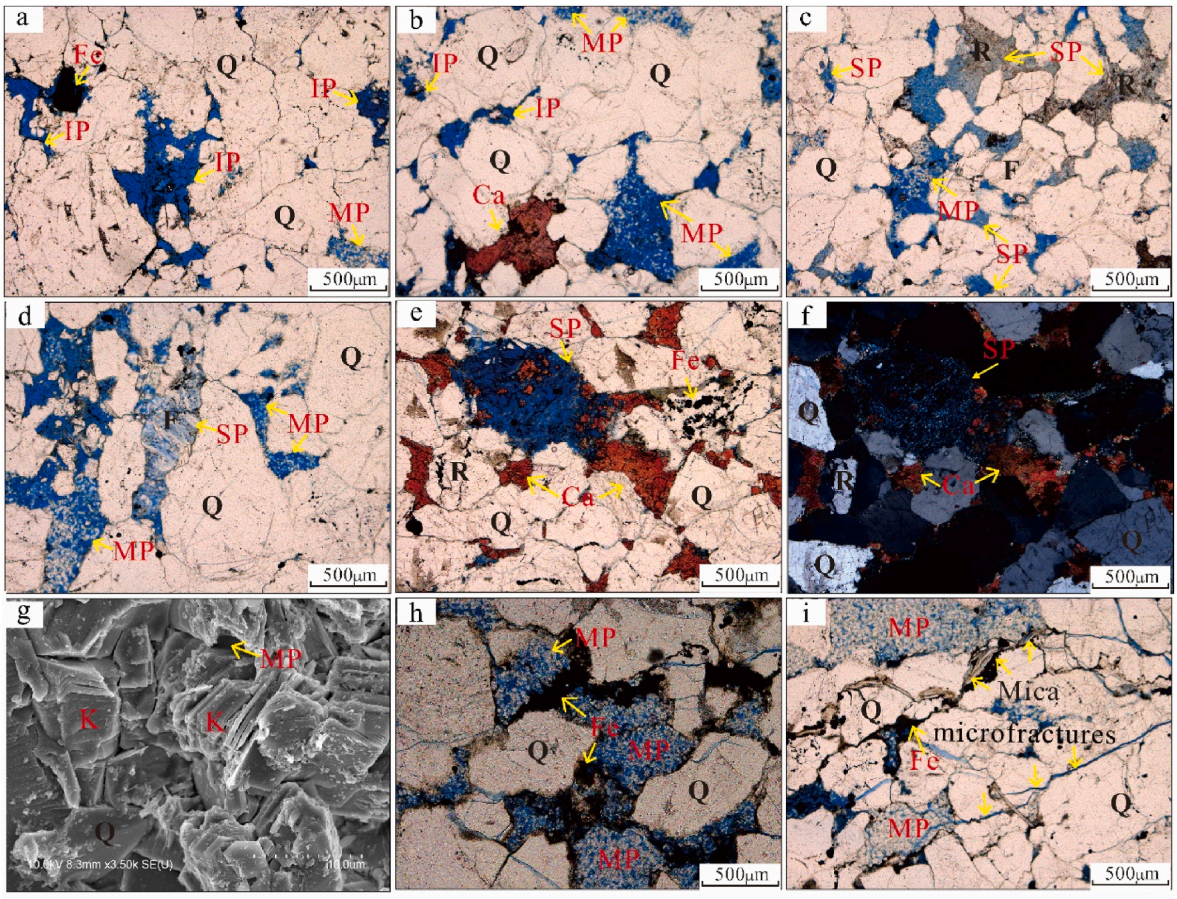


**Fig. 14.** Pore spaces of sandstone in the Benxi Formation; (a) Residual intergranular pores identified using blue epoxy resin, with Fe (blue) filling the pore spaces for sample collected from depth 2978.6 m in Well T12 (PPL). (b) Residual intergranular pores and micropores within clay aggregates, with Ca (red) filling the pore spaces for 2978.6 m in Well T12 (PPL). (c) Inter- and intragranular dissolution pores within a rock fragment for 3540.1 m in Well S426 (PPL). (d) Intragranular dissolution pores within feldspar minerals and micropores within kaolinite for 2978.6 m in Well T12 (PPL). (e–f) Pores partially filled with calcite after feldspar dissolution for Well T11 (depth, 3720.2 m) and (f) Well T11 (depth, 3720.2 m; CPL). (g) Micropores within kaolinite clay minerals for 2143.4 m in Well M51 (SEM). (h) Micropores within kaolinite clay minerals for depth 3840.6 m in Well S336 (PPL). (i) Transgranular microfractures cutting several grains for 2978.8 m in Well T12 (PPL). Notes: Ca, calcite; CPL, cross-polarized light; F, feldspar; IP, residual intergranular pores; K, kaolinite; MP, micropores; PPL, plane-polarized light; Q, quartz; R, rock fragment; SEM, scanning electron microscopy; SP, dissolution pores. (For interpretation of the references to color in this figure legend, the reader is referred to the Web version of this article.)

**Telodiagenesis**: Diagenetic evolution ceased at this stage. The burial depth was >4000 m, with some areas uplifted to approximately 3000 m. The paleogeotherm exceeded 175–200 °C, and organic matter was overmature (Ro = 2.0–4.0%) (Hu et al., 2019a). Coal-bearing rock stopped supplying hydrocarbons because the strata no longer continued to deepen; they were in weak or moderate uplift. Reservoir alkalinity gradually increased and dissolution generally stopped, and the rocks became tighter. Simultaneously, the fluid activity decreased, leading to late-stage cementation. Furthermore, suture contacts were formed between particles, primary intergranular pores rarely developed, and microfractures developed in some areas.

## 5. Discussion

### 5.1. Pore space types

Based on the occurrence and origin of Benxi Formation tight sandstone and the classification standard for tight sandstone reservoirs in China (SY/T5368-2016), the pore spaces of the sandstone are mainly secondary pores, followed by primary pores and microfractures (Jia et al., 2019a; Li et al., 2021; Hu et al., 2019a; Wang et al., 2021a).

Primary pores in the Benxi Formation sandstone are mainly residual intergranular pores that were preserved by quartz overgrowth. The pore rims are mainly flat, triangular, or polygonal; they are generally uniform in size, distribution, and connectivity (Fig. 14a and b) (Zhou et al., 2016). Secondary pores include three types: intergranular dissolution pores, intragranular dissolution pores, and micropores (sizes<0.5 μm in diameters) within clay aggregates. Intergranular dissolution pores were formed through the dissolution of grain rims or intergranular cements, creating a complex harbor-like shape (Fig. 14c) (Hu et al., 2019b; Zhou et al., 2016). Intragranular dissolution pores have a honeycomb appearance because of detrital feldspar or lithic fragment dissolution (Fig. 14d–f) (Hu et al., 2019a; Zhou et al., 2016). Detrital feldspars are generally corroded along their cleavage, and the main feldspar body is retained. Micropores within clay aggregates consist of intercrystal pores in authigenic clay minerals such as kaolinite and illite, with a honeycomb or spotted appearance (Fig. 14g and h). Thin-section and SEM analyses show that kaolinite minerals are sheet-like or laminate, ranging in size from 0.2 to 10 μm. Microfractures are also developed in the Benxi Formation because of generally high quartz content (Hu et al., 2019a; Wang et al., 2021a), which result in a brittle reservoir lithology (Fig. 14i). The fractures mainly form irregular complexes with good connectivity and long extensions.

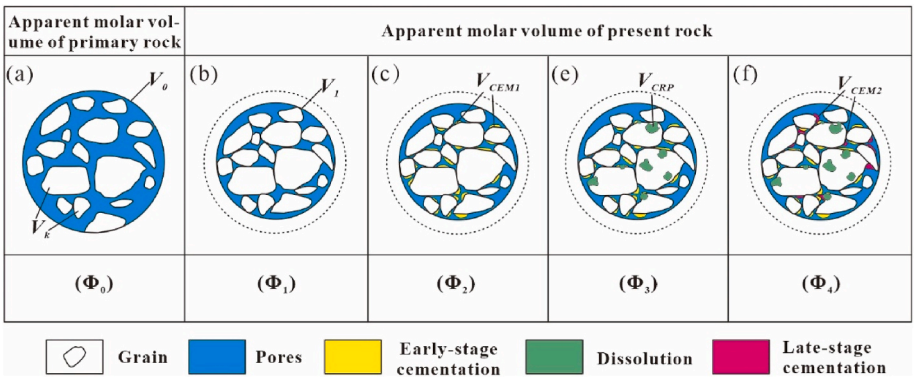


**Fig. 15.** Theoretical model of pore evolution in the Benxi Formation of the Ordos Basin, where $V_0$ is the apparent molar volume of primary pores, $V_k$ is the grain volume, $V_1$ is the apparent molar volume of present-day rock, $V_{CEM1}$ is the volume of early-stage cementation, $V_{CRP}$ is the volume of increased dissolution, and $V_{CEM2}$ is the volume of late-stage cementation.

### 5.2. Quantitative model of secondary pore formation

The diagenetic evolution of tight sandstone in the Benxi Formation can be divided into four stages according to our findings: rapid decrease in porosity after compaction during Eodiagenesis A; filling of the remaining primary pores through cementation during Eodiagenesis B; porosity increase due to dissolution during Mesodiagenesis A; and porosity loss due to secondary cementation during Mesodiagenesis B and Telodiagenesis. Based on our findings and the findings of previous studies (Beard and Weyl, 1973; Ehrenberg, 1990, 1995; Houseknecht, 1987; Hu et al., 2019a; Salman and Franks, 1993; Schmidt and McDonald, 1979; Zhang et al., 2014), this work establishes a secondary pore evolution model for tight sandstone (Fig. 15). Dissolution was the main diagenetic process in causing increased porosity in the Carboniferous Benxi Formation of the Ordos Basin, whereas strong compaction and cementation were the main factors causing a decreased reservoir porosity. Therefore, the final porosity ($\Phi$) can be obtained through a calculation of the initial porosity ($\Phi_0$), porosity loss ($\Phi_D$), and porosity increase ($\Phi_I$), as follows:

$$\Phi = \Phi_0 - \Phi_D + \Phi_I. \quad (1)$$

The determination of the initial porosity ($\Phi_0$) is the basis for analyzing the quantitative evolution of reservoir pore space, as it controls the quality of the final porosity prediction. Considering the sedimentary environment of the study area, this study adopts the initial porosity equation established by Scherer (Eq. (4)) (Scherer, 1987). The

**Table 2**
Formulae and parameters used to calculate the initial porosity ($\Phi_0$), porosity loss ($\Phi_D$), and porosity increase ($\Phi_I$).

| Porosity type | Parameter | Formula | Equation number |
|---|---|---|---|
| Initial porosity ($\Phi_0$) | Trask sorting coefficient ($S_0$) | $S_0 = \frac{\Phi_{84} - \Phi_{16}}{4} + \frac{\Phi_{95} - \Phi_5}{6.6}$ | (3) |
| | Primary porosity ($\Phi_0$) | $\Phi_0 = 20.91 + 22.9/S_0$ | (4) |
| Porosity loss ($\Phi_D$) | Intergranular volume ($\Phi_{IGV}$) | $\Phi_{IGV} = 1 - \frac{V_k}{V_1}$ | (5) |
| | Early-stage cementation content ($\Phi_{CEM1}$) | $\Phi_{CEM1} = \frac{V_{CEM1}}{V_1}$ | (6) |
| | Late-stage cementation content ($\Phi_{CEM2}$) | $\Phi_{CEM2} = \frac{V_{CEM2}}{V_1}$ | (7) |
| | Porosity loss due to compaction ($\Phi_{COPL}$) | $\Phi_{COPL} = \Phi_0 - \Phi_{IGV} \times (1 - \Phi_0) / (1 - \Phi_{IGV})$ | (8) |
| | Porosity loss due to early-stage cementation ($\Phi_{CEPL1}$) | $\Phi_{CEPL1} = \Phi_0 - \Phi_{COPL} \times \Phi_{CEM1} / \Phi_{IGV}$ | (9) |
| | Porosity loss due to late-stage cementation ($\Phi_{CEPL2}$) | $\Phi_{CEPL2} = \Phi_0 - \Phi_{COPL} \times \Phi_{CEM2} / \Phi_{IGV}$ | (10) |
| Porosity increase ($\Phi_I$) | Dissolution porosity ($\Phi_{CRP}$) | $\Phi_{CRP} = \frac{V_{CRP}}{V_1}$ | (11) |
| | Porosity increase due to dissolution ($\Phi_{CRPL}$) | $\Phi_{CRPL} = \Phi_{CRP} \times (1 - \Phi_{COPL})$ | (12) |

**Table 3**
Formulae used to calculate residual porosity after each stage of diagenesis.

| Porosity type | Formula | Equation number |
|---|---|---|
| Remaining porosity after compaction ($\Phi_1$) | $\Phi_1 = (\Phi_0 - \Phi_{COPL})/(1 - \Phi_{COPL})$ | (14) |
| Remaining porosity after early-stage cementation ($\Phi_2$) | $\Phi_2 = (\Phi_0 - \Phi_{COPL} - \Phi_{CEPL})/(1 - \Phi_{COPL})$ | (15) |
| Remaining porosity after dissolution ($\Phi_3$) | $\Phi_3 = (\Phi_0 - \Phi_{COPL} - \Phi_{CEPL1} + \Phi_{CRPL})/(1 - \Phi_{COPL})$ | (16) |
| Remaining porosity after late-stage cementation ($\Phi_4$) | $\Phi_4 = (\Phi_0 - \Phi_{COPL} - \Phi_{CEPL1} + \Phi_{CRPL} - \Phi_{CEPL2})/(1 - \Phi_{COPL})$ | (17) |

Trask sorting coefficient ($S_0$) was calculated in accordance with the widely used Folk and Ward formula (Eq. (3)) (Folk, 1957).

To obtain the porosity loss ($\Phi_D$), this work assumes that the diagenesis processes causing a reduced porosity in the Benxi Formation arere mainly compaction and cementation, based on our thin-section analyses and diagenesis model. We used separate formulae to calculate porosity loss due to compaction (Eq. (8)) and cementation (Eqs. (9) and (10)), based on previous studies and the theoretical model shown in Fig. 15. As the diagenesis process causing an increased porosity in the Benxi Formation is mainly dissolution, thus, the porosity increase ($\Phi_I$) is calculated as the porosity increase due to dissolution ($\Phi_{CRPL}$) as below:

$$\Phi_D = \Phi_{COPL} + \Phi_{CEPL1} + \Phi_{CEPL2}. \quad (2)$$

The formulae and detailed parameters used to obtain the initial porosity, porosity loss, and porosity increase are listed in Table 2 (Beard and Weyl, 1973; Houseknecht, 1987; Paxton et al., 2002; Hu et al., 2019a; Zhang et al., 2014).

$\Phi_5$, $\Phi_{16}$, $\Phi_{84}$, and $\Phi_{95}$ are intercepts that correspond to cumulative quantiles of 5, 16, 84, and 95 on cumulative probability curves, respectively. $V_k$ is the grain volume; $V_1$ is the apparent molar volume of present-day rock; $V_{CEM1}$ is the volume of early-stage cementation; $V_{CRP}$ is the volume increase due to dissolution; $V_{CEM2}$ is the volume of late-stage cementation.

The residual porosity after each diagenetic stage can also be obtained using formulae listed in Table 3. The remaining porosity after late-stage cementation ($\Phi_4$) is the final porosity ($\Phi$):

$$\Phi_4 = \Phi. \quad (13)$$

Thus, we calculated the porosity loss due to compaction and cementation and the porosity increase due to dissolution for a total of 23 wells, according to data from the thin-section analyses of tight sandstone reservoirs of the Carboniferous Benxi Formation in the Ordos Basin (Table 4). Porosity loss after compaction ranges from 22.7% to 36.0%

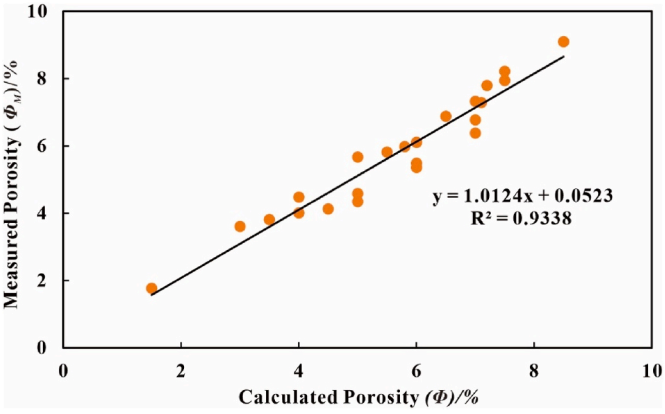


**Fig. 16.** Correlation between calculated and measured porosity values for the Benxi Formation.

**Table 4**
Porosity losses due to compaction and cementation and increases due to dissolution in tight sandstone reservoirs of the Benxi Formation.

| Well | Depth (m) | $\Phi_0$ (%) | $\Phi_{COPL}$ (%) | $\Phi_{CEPL1}$ (%) | $\Phi_{CRPI}$ (%) | $\Phi_{CEPL2}$ (%) | $\Phi$ (%) | $\Phi_M$ (%) |
|---|---|---|---|---|---|---|---|---|
| S99 | 1969.3 | 43.0 | 38.0 | 3.7 | 1.2 | 4.6 | 7.5 | 7.9 |
| M51 | 2160.3 | 41.0 | 34.3 | 4.3 | 2.2 | 4.2 | 6.5 | 6.8 |
| S13 | 2275.2 | 40.0 | 36.1 | 2.8 | 0.9 | 3.5 | 5.5 | 5.8 |
| S51 | 2329.2 | 42.5 | 37.5 | 3.7 | 1.2 | 4.5 | 7.2 | 7.8 |
| M35 | 2537.1 | 43.5 | 39.8 | 2.4 | 1.2 | 3.4 | 5.8 | 5.9 |
| M9 | 2751.6 | 44.0 | 38.4 | 4.3 | 1.2 | 3.0 | 5.0 | 4.3 |
| M38 | 2784.8 | 45.0 | 28.5 | 10 | 6.4 | 2.8 | 4.0 | 4.0 |
| Z8 | 2937.0 | 43.0 | 38.0 | 3.7 | 1.2 | 2.7 | 4.5 | 4.1 |
| T12 | 2978.1 | 42.5 | 35.5 | 5.4 | 1.5 | 3.2 | 5.0 | 5.6 |
| S218 | 3021.4 | 39.0 | 35.7 | 2.2 | 0.9 | 5.4 | 8.5 | 9.1 |
| Q17 | 3027.0 | 39.0 | 24.0 | 12.1 | 2.8 | 5.3 | 7.0 | 7.3 |
| S468 | 3176.8 | 40.5 | 35.3 | 3.8 | 1.2 | 3.2 | 5.0 | 4.5 |
| Z54 | 3235.5 | 37.0 | 33.3 | 2.6 | 1.0 | 4.6 | 7.0 | 6.3 |
| S434 | 3533.5 | 42.0 | 33.3 | 5.3 | 3.3 | 5.0 | 7.5 | 8.2 |
| S435 | 3542.3 | 38.0 | 28.2 | 4.2 | 5.4 | 5.0 | 7.1 | 7.2 |
| S322 | 3557.1 | 43.0 | 38.0 | 3.4 | 1.5 | 3.7 | 6.0 | 5.4 |
| S315 | 3651.0 | 45.0 | 42.7 | 1.6 | 0.6 | 2.0 | 3.5 | 3.8 |
| T11 | 3719.7 | 42.5 | 36.8 | 4.1 | 1.5 | 0.9 | 1.5 | 1.7 |
| S427 | 3739.6 | 36.0 | 31.9 | 3.0 | 1.0 | 4.0 | 6.0 | 6.1 |
| S336 | 3829.4 | 37.0 | 28.5 | 6.3 | 2.0 | 2.8 | 4.0 | 4.4 |
| S215 | 3891.5 | 43.0 | 35.9 | 4.8 | 2.2 | 4.4 | 7.0 | 6.7 |
| S396 | 3907.5 | 41.0 | 37.2 | 2.5 | 1.2 | 1.8 | 3.0 | 3.61 |
| L45 | 4014.9 | 39.5 | 36.3 | 2.2 | 0.9 | 3.8 | 6.0 | 5.3 |
| Mean | | 39.9 | 34.9 | 4.3 | 1.8 | 3.6 | 4.1 | 5.7 |

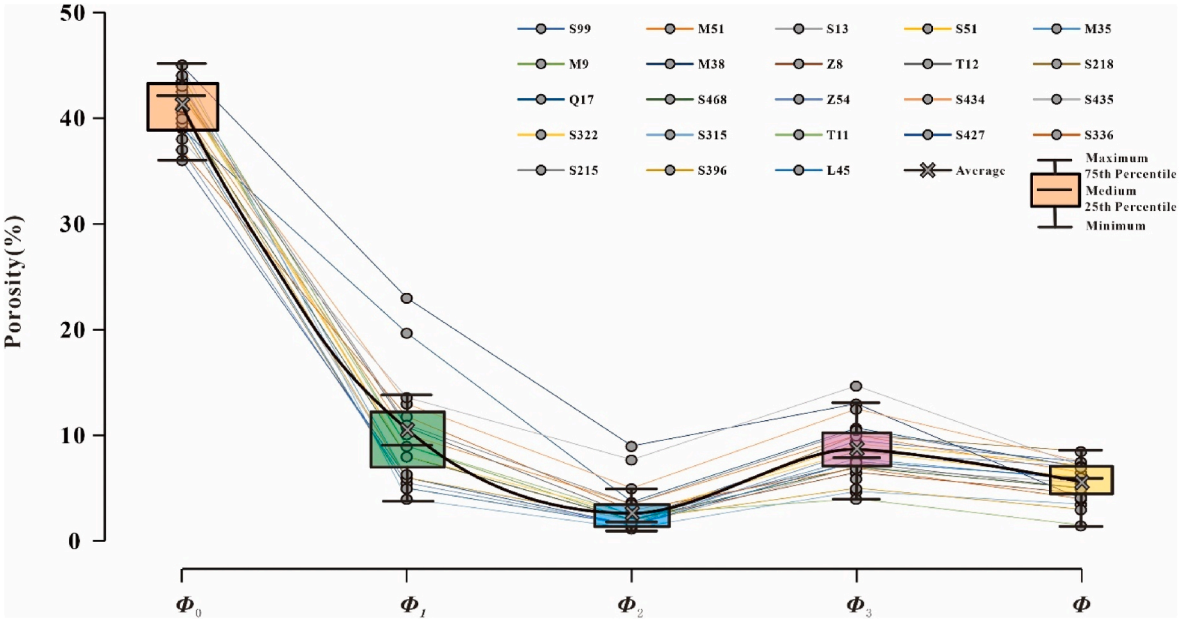


**Fig. 17.** Calculated porosities of Benxi Formation reservoirs at different evolutionary stages. $\Phi_0$ is initial porosity; $\Phi_1$ is porosity remaining after compaction; $\Phi_2$ is porosity remaining after early-stage cementation; $\Phi_3$ is porosity remaining after dissolution; $\Phi$ is final calculated porosity.

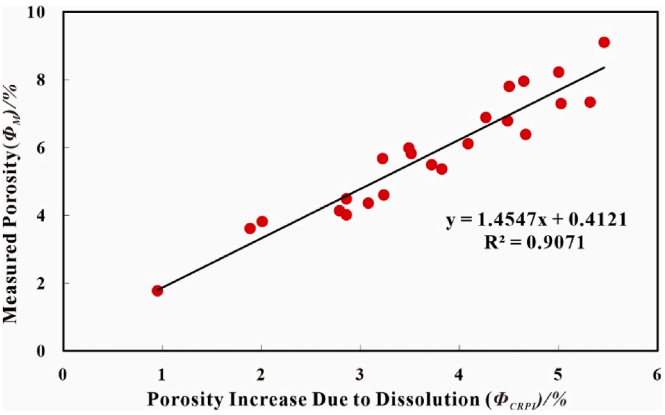


**Fig. 18.** Correlation between the porosity increase due to dissolution and the measured porosity.

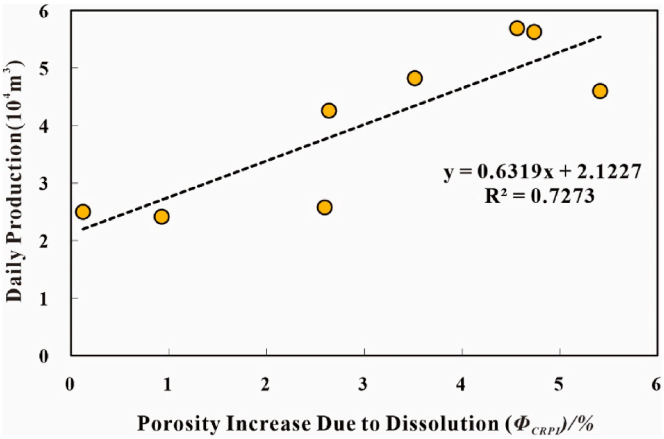


**Fig. 19.** Scatter plot showing the relationship between the porosity increase due to dissolution and the daily production in the Benxi Formation.

(mean, 32.5%). The porosity loss due to cementation varies from 2.6% to 10.8% (mean, 4.8%). The porosity increase due to dissolution changes from 1.0% to 5.4% (mean, 3.6%). The calculated final porosity is from 3.0% to 8.5% (mean, 4.1%), and the measured porosity alters from 3.6% to 8.2% (mean, 5.7%). The present-day porosity values calculated using the model are closely correlated with measured porosity values (Fig. 16).

$\Phi_0$ is the initial porosity; $\Phi_{COPL}$ is porosity loss due to compaction; $\Phi_{CEPL1}$ is porosity loss due to early-stage cementation; $\Phi_{CRPI}$ is porosity increase due to dissolution; $\Phi_{CEPL2}$ is porosity loss due to late-stage cementation; $\Phi$ is final calculated porosity; $\Phi_M$ is measured porosity.

### 5.3. Recovery of the pore evolution process

Our porosity evolution calculation results for the tight sandstone reservoir of the Benxi Formation (Fig. 17) show that the sandstone is tight after early-stage compaction (mean, 10.6%) and fully tight after early-stage cementation (porosity <10%). Dissolution is the factor that most strongly improves the reservoir, increasing porosity by up to 40–250% prior to dissolution. The degree of porosity evolution varies

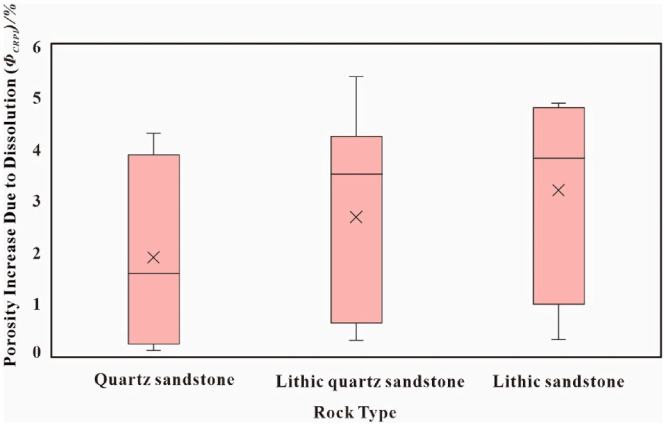


**Fig. 20.** Porosity increases due to dissolution in different rock types of the Benxi Formation.

regionally. Deeper burial is associated with stronger compaction (Wells S336 and S215), whereas shallower burial is linked with stronger cementation (Wells M38 and Q17).

The Benxi Formation reservoir has experienced early rapid and continuous burial, along with late weak tectonic uplift, which led to strong compaction (Jia et al., 2019a; Li et al., 2021; Hu et al., 2019a). The reservoir was rapidly tightened under the combined effects of compaction and early-stage cementation. Dissolution was an important transformation effect in this region, contributing to greater porosity (Hu et al., 2019a). A clear positive correlation between the porosity increase due to dissolution and the measured porosity is noted (Fig. 18); therefore, dissolution is presumably the main factor that controls the "sweet spot."

### 5.4. Factors controlling secondary pore development

Multiple mechanisms complexly influence the development of secondary pore space, such as meteoric water flushing, formation of authigenic clay minerals, facies migration and leaching of feldspars, rock fragments and carbonate cements (Bloch and Franks, 1993; Qiu et al., 2002; Dou et al., 2017). Lai et al. (2015) reported that more secondary pore space developed in mouthbar or underwater distributary channel facies. Additionally, facies-controlled detrital components can critically influence the reservoir quality and secondary pore of sandstones by conditioning the pathway of both physical and chemical diagenesis (Rossi et al., 2001). Zhu et al. (2015) pay much attention to alkaline dissolution of quartz, arguing that development of significant secondary porosity is related to dissolution of quartz. Whereas others regard the leaching of feldspars, rock fragments and carbonate cements by acidic fluids (Giles and Marshall, 1986), emphasizing the importance of leaching of unstable minerals. Shirley et al. (2010) reported that volume of secondary pores remains nearly constant during deep burial, because volume of this late dissolution of potassium feldspar is offset by precipitation of ankerite, albite, illite, and minor quartz in secondary pores. In the 1970s and 1980s, several papers (Surdam et al., 1989; Yuan et al., 2015a,b); proposed that organic acid and carbon dioxide dissolution of carbonate and feldspar can produce secondary pores. Secondary pores in the tight sandstone of the Benxi Formation were mainly derived through the dissolution of soluble components within the rock fragments and early-stage carbonate cements. Our quantitative results for secondary pores in the Benxi Formation show that the porosity increase due to dissolution had a positive effect on the physical properties of the tight sandstone reservoir (Fig. 19), thus partially controlling the distribution of the "sweet spot." Secondary pores are mainly produced through the dissolution of mineral grains and fillings by acidic fluids. Therefore, to clarify the factors controlling secondary pore development, below we focus on the discussion of reservoir types, diagenetic fluid properties, and hydrocarbon source rocks in the Benxi Formation.

#### 5.4.1. Effect of lithology on secondary pore development

Three rock types developed in the Benxi Formation include quartz sandstone, lithic quartz sandstone, and lithic sandstone (Dutton and Loucks, 2010; Hu et al., 2019a; Wang et al., 2021a). Most components of rock fragments including potassium feldspar, sodium feldspar, calcite, and biotite are unstable during early Mesodiagenesis, which is accompanied by the formation of organic acids. For example, potassium feldspar can be converted to clay minerals and quartz cements in an acidic environment, as follows (Li et al., 2020):

$$2KAlSi_3O_8(K-feldspar)+CH_3COOH+H_2O+2O_2 \rightarrow Al_2Si_2O_5(OH)_4(kaolinite)+4SiO_2(quartz)+2K^+ +2HCO_32HCO_3^- \quad (18)$$

Thus, quartz is formed during dissolution; in sandstone with high quartz content, the quartz surface is more exposed and new quartz is more likely to be deposited on the rims of old quartz grains. Accordingly, more mature sandstone (e.g., quartz sandstone) is associated with greater quartz overgrowth (Zahid et al., 2016). In contrast, both immature sandstone (e.g., lithic quartz sandstone and lithic sandstone) and poor primary pore development are associated with easier inter- and intra-granular dissolution of unstable minerals under an acidic fluid action, leading to secondary pore development. Considering the established model of secondary pore evolution, the increased secondary pore space observed among different rock types confirms this conclusion (Fig. 20). Lithic sandstone shows the highest increase in porosity due to dissolution, followed by the lithic quartz sandstone and quartz sandstone. Therefore, a less mature sandstone composition leads to a higher soluble fraction and partially favors the formation of secondary pore space.

#### 5.4.2. Effect of diagenetic fluid on secondary pore development

Reservoirs are modified by diagenesis during burial. Diagenesis produces large amounts of acidic fluids and hydrocarbons in the hydrocarbon generation process, which affect pH, Eh, and other physical and chemical conditions of the pore fluids in the reservoir adjacent to the hydrocarbon source rock. In addition, diagenesis also causes ions within minerals to enter the fluid and dissolve, cement, or replace other

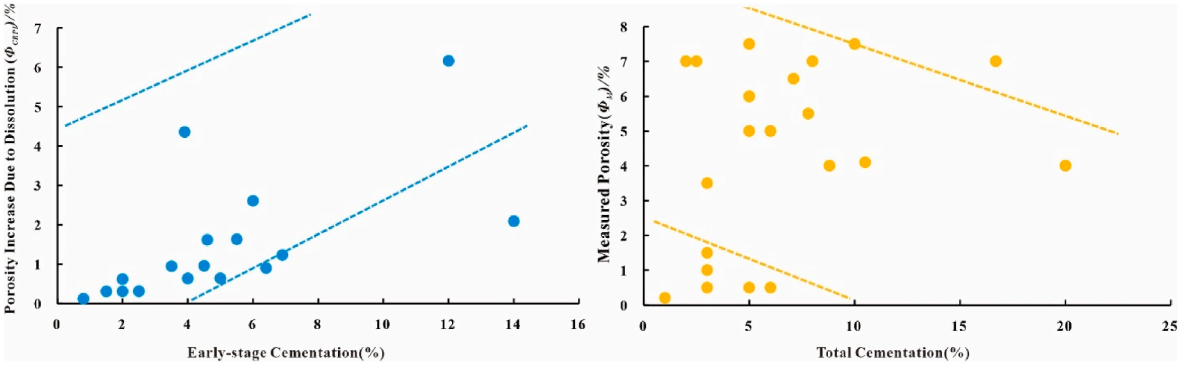


**Fig. 21.** Relationships between early cementation and porosity increase due to dissolution (Left), and between total cementation and measured porosity (Right).

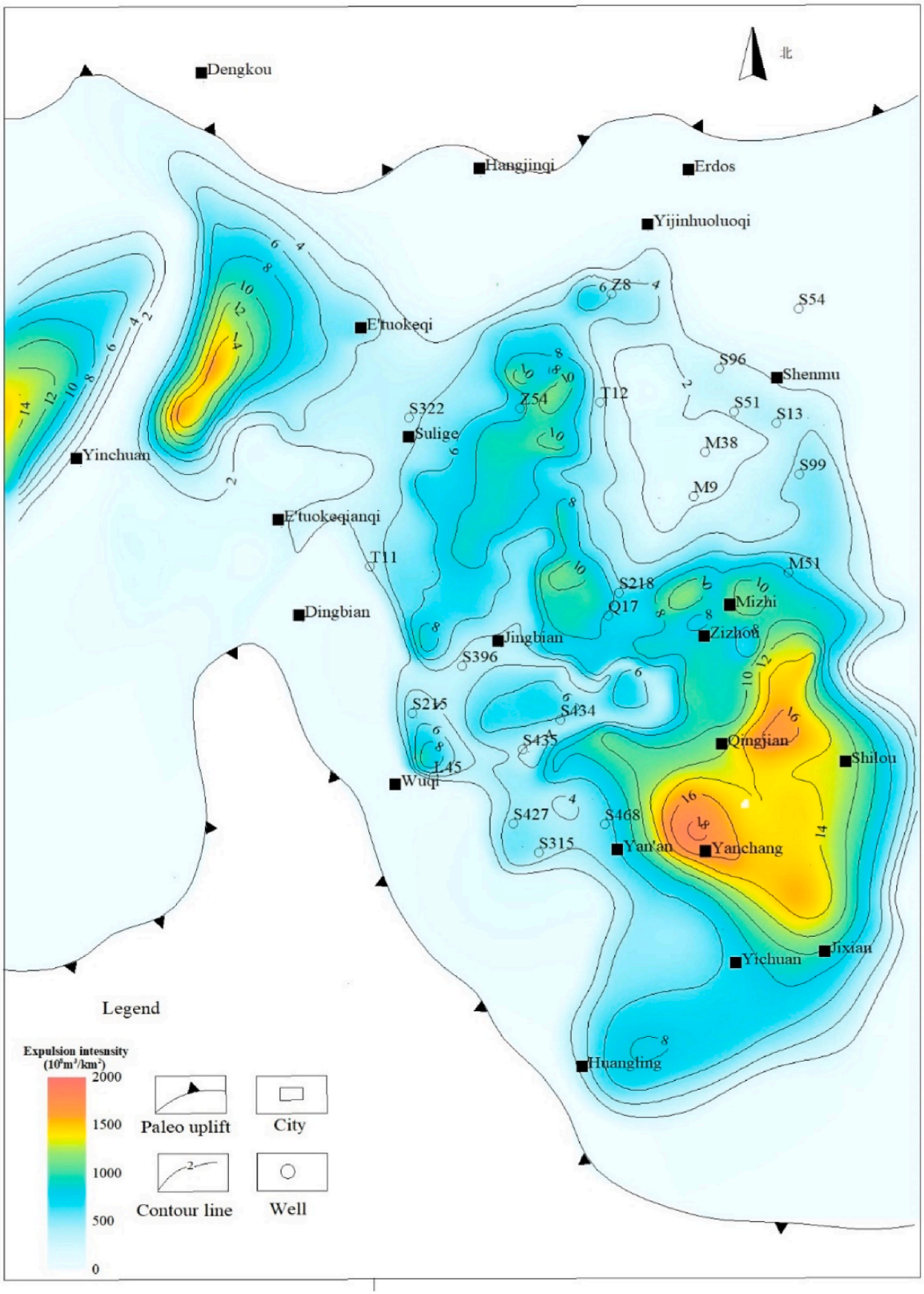


**Fig. 22.** Hydrocarbon expulsion intensity map with sampling wells of the Benxi Formation in the Ordos Basin.

minerals. Fluid properties are closely related to secondary pore development, which directly affects the physical properties of the reservoir. For example, $H^+$ is released during the conversion of kaolinite to illite, thereby lowering the fluid pH as Eq. (19) (Morad et al., 2010; Yuan et al., 2015a,b):

$$3Al_2Si_2O_5(OH)_4(kaolinite) + 2K^+ \rightarrow 2KAl_3Si_3O_{10}(OH)_2(illite) + 2H^+ + 3H_2O \quad (19)$$

$H^+$ is also released by early carbonate cementation as Eq. (20) (Yuan

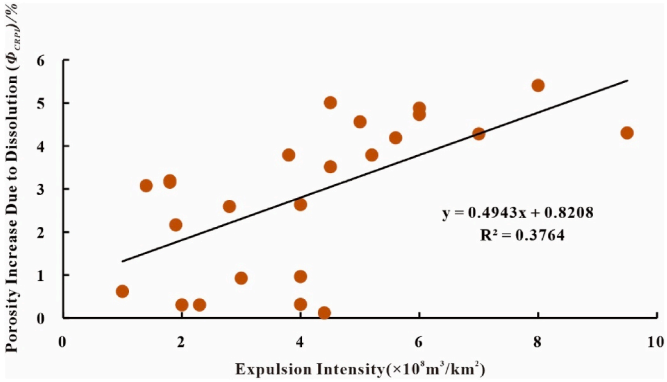


**Fig. 23.** Relationship between hydrocarbon expulsion intensity and porosity increase due to dissolution in the Benxi Formation.

et al., 2015a,b):

$$Ca^{2+} + CO_2(g) + H_2O \rightarrow CaCO_3(calcite) + H^+ \quad (20)$$

These effects collectively intensify reservoir dissolution; early carbonate cement is also dissolved by organic acids at a later stage (Crundwell, 2014; Panagiotopoulou et al., 2007). Some studies have shown that quartz cements experience a partial dissolution in alkaline environments during late diagenesis. An assessment of the relationship between early cementation and porosity increase due to dissolution in sandstone within the Benxi Formation reveals a positive correlation, whereby early cementation controls the degree of reservoir dissolution (Fig. 21). However, the cement content continues to increase as the pore formation process evolves, thereby forming crystalline cementation to block the pore space of the reservoir, while inhibiting the flow of acidic fluids and reservoir modification; overall, these changes result in reservoir densification. Consequently, although early carbonate cement produced during diagenesis promotes a secondary pore development, the total amount of cements produced will degrade their physical properties.

#### 5.4.3. *Effect of organic source on secondary pore development*

It is commonly accepted that silicate minerals and carbonates are dissolved by organic acids in hydrocarbon reservoirs. The dissolution of soluble minerals in a reservoir by organic acids released during the thermal evolution of organic matter is an important mechanism for the generation of secondary dissolution pores during the diagenesis of clastic reservoirs (Panagiotopoulou et al., 2007). Organic acids are formed by decarboxylation during the maturation of organic matter (Yuan et al., 2019a, 2019b). Greater hydrocarbon discharge intensity from hydrocarbon source rocks is associated with higher organic acid production, which is more favorable for secondary pore formation. Because of the variable burial depths of the Benxi Formation strata and the diverse temperature-pressure conditions in each area, the degree of thermal evolution of hydrocarbon source rocks (coal seams) varies, and the intensity of hydrocarbon generation and expulsion also varies (Fig. 22). The hydrocarbon expulsion center of the study area is located in the southern region, where organic acid is more abundant. Indeed, a scatter plot of hydrocarbon expulsion intensity and porosity increase due to dissolution shows a significant positive correlation (Fig. 23).

## 6. Conclusion

The Benxi Formation has experienced four stages of diagenesis and associated pore development: rapid decrease in porosity after compaction during Eodiagenesis A; filling of the remaining primary pores through cementation during Eodiagenesis B; porosity increase due to dissolution during Mesodiagenesis A; and porosity loss due to secondary cementation during Mesodiagenesis B and Telodiagenesis. At present, the Benxi Formation is mainly in the Mesodiagenesis B stage, and partly in Telodiagenesis.

Using quantitative thin-section porosity analyses, based on an initial porosity recovery model and pore evolution parameters in the literature, this work determines that the original porosity of sandstone in the Benxi Formation was 39.8% and the increase in porosity due to dissolution was 1.0–5.4% with a mean of 4.1%; this constituted 40–250% of the porosity before dissolution.

Rock types, diagenetic fluid properties, and source rocks all influence the development of secondary dissolved pores in the study area. Lithic sandstone and lithic quartz sandstone with low compositional maturity show a stronger dissolution, compared with quartz sandstone. Acidic fluid formed through calcareous cementation, whereas illite promoted dissolution; in addition, alkaline fluid in the late diagenetic stage also dissolved siliceous cements. Organic acids under the control of hydrocarbon expulsion has a positive effect on dissolution. Greater hydrocarbon expulsion intensity lead to greater pore dissolution. Overall, these three factors have practical significance for the prediction and exploration of gas “sweet spots” in the tight sandstone of the Benxi Formation.

## Declaration of competing interest

The authors declare that they have no known competing financial interests or personal relationships that could have appeared to influence the work reported in this paper.

## Data availability

Data will be made available on request.

## Acknowledgements

This study received support from the Youth Program of the National Natural Science Foundation of China (Grant No.41802148). Financial support from the China Scholarship Council (CSC) and American Association of Petroleum Geologists (AAPG) Grants-in-Aid are gratefully acknowledged. We would like to thank anonymous reviewers for their invaluable suggestions.

## References

Amel, H., Jafarian, A., Husinec, A., Koeshidayatullah, A., Swennen, R., 2015. Microfacies, depositional environment and diagenetic evolution controls on the reservoir quality of the permian upper dalan formation, kish gas field, zagros basin. Mar. Petrol. Geol. 67, 57–71.

Bai, L.H., Liu, B., Yang, J., Tian, S., Wang, B.Y., Huang, S., 2021. Differences in hydrocarbon composition of shale oils in different phase states from the Qingshankou Formation, Songliao Basin, as determined from fluorescence experiments. Front. Earth Sci. 15, 438–456.

Bai, L.H., Liu, B., Du, Y.J., Wang, B.Y., Tian, S.S., Wang, L., Xue, Z.Q., 2022. Distribution characteristics and oil mobility thresholds in lacustrine shale reservoir: insights from N2 adsorption experiments on samples prior to and following hydrocarbon extraction. Petrol. Sci. 19, 486–497.

Beard, D., Weyl, P., 1973. Influence of texture on porosity and permeability of unconsolidated sand. AAPG Bull. 57, 349–369.

Colón, C.F.J., Oelkers, E.H., Schott, J., 2004. Experimental investigation of the effect of dissolution on sandstone permeability, porosity, and reactive surface area. Geochem. Cosmochim. Acta 68, 805–817.

Crundwell, F., 2014. The mechanism of dissolution of minerals in acidic and alkaline solutions: Part II Application of a new theory to silicates, aluminosilicates and quartz. Hydro 149, 265–275.

Dai, J.X., Ni, Y.Y., Dong, D.Z., Qin, S.F., Zhu, G.Y., Huang, S.P., Yu, C., Gong, D.Y., Hong, F., Zhang, Y.L., 2021. 2021-2025 is a period of great development of China’s natural gas industry: suggestions on the exploration and development of natural gas during the 14th five-year plan in China. J. Nat. Gas Geo. 6, 183–197.

Dou, W.C., Liu, L.F., Wu, K.J., Xu, Z.J., Feng, X., 2017. Origin and significance of secondary porosity: a case study of upper Triassic tight sandstones of Yanchang Formation in Ordos basin, China. J. Petrol. Sci. Eng. 149, 485–496.

Dutton, S.P., Loucks, R.G., 2010. Diagenetic controls on evolution of porosity and permeability in lower Tertiary Wilcox sandstones from shallow to ultradeep (200–6700 m) burial, Gulf of Mexico Basin, USA. Mar. Petrol. Geol. 27 (1), 69–81.

Ehrenberg, S., 1990. Relationship between diagenesis and reservoir quality in sandstones of the Garn Formation, Haltenbanken, mid-Norwegian continental shelf. AAPG Bull. 74, 1538–1558.
Ehrenberg, S., 1995. Measuring sandstone compaction from modal analyses of thin sections; how to do it and what the results mean. J. Sediment. Res. 65, 369–379.
Ehrenberg, S., Nadeau, P., Steen, Ø., 2009. Petroleum reservoir porosity versus depth: influence of geological age. AAPG Bull. 93, 1281–1296.
Folk, W., 1957. Astudyinthesignificanceofgrainsize parameters. J. Sediment. Petrol. 27, 3–27.
Gier, S., Worden, R.H., Johns, W.D., Kurzweil, H., 2008. Diagenesis and reservoir quality of miocene sandstones in the vienna basin, Austria. Mar. Petrol. Geol. 25, 681–695.
Giles, M.R., Marshall, J.D., 1986. Constraints on the development of secondary porosity in the subsurface: re-evaluation of processes. Mar. Petrol. Geol. 3 (3), 243–255.
Hong, D.D., Cao, J., Wu, T., Dang, S.S., Hu, W.X., Yao, S.P., 2020. Authigenic clay minerals and calcite dissolution influence reservoir quality in tight sandstones: insights from the central Junggar Basin, NW China. Energy Geosci 1, 8–19.
Houseknecht, D.W., 1987. Assessing the relative importance of compaction processes and cementation to reduction of porosity in sandstones. AAPG Bull. 71, 633–642.
Hu, P., Yu, X.H., Cao, H.L., 2019a. Characteristics and a quantitative diagenetic porosity evolution mode of barrier bar sandstone reservoirs: a case study of the Benxi Formation, Yanchang exploration block, Ordos Basin. Acta Sedimentol. Sin. 37, 390–402 (in Chinese with English abstract).
Hu, Y.Y., Pang, X.Q., Jiang, F.J., Li, L., Zheng, D.Y., Shao, X.H., 2019b. Coupling relationship between tight sandstone reservoir and gas charging: an example from lower Permian Taiyuan Formation in Kangning field, northeastern Ordos Basin, China. Mar. Petrol. Geol. 105, 238–250.
Jia, L.B., Zhong, D.K., Ji, Y.L., Zhou, Y., Liu, J.L., Mi, L.J., Li, D.J., Yan, R.T., Yi, Z., Jia, L. K., 2019a. Architecture of tectonic sequences, depositional systems, and tectonic controls of the sedimentary fills of the rift-related Wenchang Formation in the Lufeng Depression, Pearl River Mouth Basin, China. Geol. J. 54, 1950–1975.
Jia, L.B., Zhong, D.K., Sun, H., Yan, R., Zhang, C.L., Mo, W.L., Qiu, C., Dong, Y., Li, B., Liao, G., 2019b. Sediment provenance analysis and tectonic implication of the Benxi Formation, Ordos Basin. Acta Sedimentol. Sin. 13, 1038–1050 (in Chinese with English abstract).
Jiang, F.J., Zhang, C.L., Wang, K., Zhao, Z.F., Zhong, K., 2019. Characteristics of micropores, pore throats, and movable fluids in the tight sandstone oil reservoirs of the Yanchang Formation in the southwestern Ordos Basin, China. AAPG Bull. 103, 2835–2859.
Lai, J., Wang, G.W., Ran, Y., Zhou, Z.L., 2015. Predictive distribution of high-quality reservoirs of tight gas sandstones by linking diagenesis to depositional facies: evidence from Xu-2 sandstones in the Penglai area of the central Sichuan basin, China. J. Nat. Gas Sci. Eng. 23, 97–111.
Li, J., Luo, X., 2005. Natural gas accumulation in the upper paleozoic of Ordos Basin, China. Petrol. Explor. Dev. 32, 54.
Li, Y., Xu, W.K., Wu, P., Meng, S.Z., 2020. Dissolution versus cementation and its role in determining tight sandstone quality: a case study from the Upper Paleozoic in northeastern Ordos Basin, China. J. Nat. Gas Sci. Eng. 78, 103324.
Li, J., Zhang, C.L., Jiang, F.J., Pei, Y., Wang, J.Y., Wang, X.R., Zhang, J.Q., 2021. Main factors controlling the enrichment of upper caiboniferous Benxi Formation tight gas in the Ordos Basin. Nat. Gas. Ind. 41, 30–40 (in Chinese with English abstract).
Li, G.X., Lei, Z.D., Dong, W.H., Wang, H.Y., Zheng, X.F., Tan, J., 2022. Progress, challenges and prospects of unconventional oil and gas development of CNPC. China Petrol. Explor. 27, 1 (in Chinese with English abstract).
Morad, S., Al-Ramadan, K., Ketzer, J.M., De Ros, L., 2010. The impact of diagenesis on the heterogeneity of sandstone reservoirs: a review of the role of depositional facies and sequence stratigraphy. AAPG Bull. 94, 1267–1309.
Nedkvitne, T., Karlsen, D.A., Bjørlykke, K., Larter, S.R., 1993. Relationship between reservoir diagenetic evolution and petroleum emplacement in the Ula Field, North Sea. Mar. Petrol. Geol. 10, 255–270.
Nelson, P.H., 2009. Pore-throat sizes in sandstones, tight sandstones, and shales. AAPG Bull. 93, 329–340.
Oluwadebi, A.G., Taylor, K.G., Ma, L., 2019. A case study on 3D characterisation of pore structure in a tight sandstone gas reservoir: the Collyhurst Sandstone, East Irish Sea Basin, northern England. J. Nat. Gas Sci. Eng. 68, 102917.
Panagiotopoulou, C., Kontori, E., Perraki, T., Kakali, G., 2007. Dissolution of aluminosilicate minerals and by-products in alkaline media. J. Mat. Sci. 42, 2967–2973.
Paxton, S., Szabo, J., Ajdukiewicz, J., Klimentidis, R., 2002. Construction of an intergranular volume compaction curve for evaluating and predicting compaction and porosity loss in rigid-grain sandstone reservoirs. AAPG Bull. 86, 2047–2067.
Petrol, B., 2021. BP Statistical Review of World Energy July 2021.
Pokrovsky, O.S., Golubev, S.V., Schott, J., Castillo, A., 2009. Calcite, dolomite and magnesite dissolution kinetics in aqueous solutions at acid to circumneutral pH, 25 to 150 C and 1 to 55 atm pCO2: new constraints on CO2 sequestration in sedimentary basins. Chem. Geol. 265, 20–32.
Qiu, L.W., Qiu, R.H., Jiang, Z.X., Chen, W.X., Cao, Y.C., 2002. Alkaline diagenesis and its influence on a reservoir in the Biyang depression, 2002 Sci. China Earth Sci. 45 (7), 643–653 (in Chinese with English abstract).
Qiu, Z.J., Zhao, W.Z., Hu, S.Y., Zhang, G.S., Fang, H., 2011. The natural gas resource potential and its important status in the coming low-carbon economy. Eng. Sci. 13, 81–86 (in Chinese with English abstract).
Rossi, C., Marfil, R., Ramseyer, K., Permanyer, A., 2001. Facies-related diagenesis and multiphase siderite cementation and dissolution in the reservoir sandstones of the Khatatba Formation, Egypt's western desert. J. Sediment. Res. 71 (3), 459–472.
Salman, B., Franks, S.G., 1993. Preservation of shallow plagioclase dissolution porosity during burial: implications for porosity prediction and aluminum mass balance. AAPG Bull. 77 (9), 1488–1501.
Scherer, M., 1987. Parameters influencing porosity in sandstones: a model for sandstone porosity prediction. AAPG Bull. 71, 485–491.
Schmidt, V., McDonald, D.A., 1979. The Role of Secondary Porosity in the Course of Sandstone Diagenesis. SEPM Special Publication No. 26, Tulsa, Oklahoma.
Su, N.N., Song, F., Qiu, L.W., Zhang, W., 2021. Diagenetic evolution and densification mechanism of the upper paleozoic tight sandstones in the Ordos Basin, northern China. J. Asian Earth Sci. 205, 104613.
Sun, L.D., Zou, C.N., Jia, A.L., Wei, Y.S., Zhu, R.K., Wu, S.T., Guo, Z., 2019. Development characteristics and orientation of tight oil and gas in China. Petrol. Explor. Dev. 46, 1073–1087.
Surdam, R.C., Crossey, L.J., Hagen, E.S., Heasler, H.P., 1989. Organic-inorganic interactions and sandstone diagenesis. AAPG Bull. 73, 1–23.
Taylor, T.R., Giles, M.R., Hathon, L.A., Diggs, T.N., Braunsdorf, N.R., Birbiglia, G.V., Kittridge, M.G., Macaulay, C.I., Espejo, I.S., 2010. Sandstone diagenesis and reservoir quality prediction: models, myths, and reality. AAPG Bull. 94, 1093–1132.
Wang, J.Y., Jiang, F.J., Zhang, C.L., Song, Z.Z., Mo, W.L., 2021a. Study on the pore structure and fractal dimension of tight sandstone in coal measures. Energy Fuel. 35, 3887–3898.
Wang, J., Zhang, C.L., Li, J., 2021b. Tight sandstone gas reservoirs in the Sulige gas field: development understandings and stableproduction proposals. Nat. Gas. Ind. 41, 100–110 (in Chinese with English abstract).
Wang, Q.M., Hu, Q.H., Ning, X.W., Ilavsky, J., Kuzmenko, I., Tom, T., 2021c. Spatial heterogeneity analyses of pore structure and mineral composition of Barnett Shale using X-ray scattering techniques. Mar. Petrol. Geol. 134, 105354.
Yang, X.G., Guo, S.B., 2020a. Porosity model and pore evolution of transitional shales: an example from the Southern North China Basin. Petrol. Sci. 17, 1512–1526.
Yang, X.G., Guo, S.B., 2020b. Comparative analysis of shale pore size characterization methods. Petrol. Sci. Technol. 38, 793–799.
Yang, X.G., Guo, S.B., 2021. Reservoirs characteristics and environments evolution of lower permian transitional shale in the Southern North China Basin: implications for shale gas exploration. J. Nat. Gas Sci. Eng. 96, 104282.
Yang, R.C., Fan, A.P., Han, Z.Z., Wang, X.P., 2012. Diagenesis and porosity evolution of sandstone reservoirs in the East II part of Sulige gas field, Ordos Basin. Int. J. Min. Sci. Technol. 22, 311–316.
Yang, S.F., Bao, Z.D., Wang, N., Qu, X.F., Lin, Y.B., Shen, J.J., Awan, R.S., 2020. Diagenetic evolution and its impact on reservoir quality of tight sandstones: a case study of the Triassic Chang 6 Member, Ordos Basin, northwest China. Mar. Petrol. Geol. 117, 104360.
Yuan, G.H., Cao, Y.C., Gluyas, J., Li, X.Y., Xi, K.L., Wang, Y.Z., Jia, Z.Z., Sun, P.P., Oxtoby, N.H., 2015a. Feldspar dissolution, authigenic clays, and quartz cements in open and closed sandstone geochemical systems during diagenesis: typical examples from two sags in Bohai Bay Basin, East China. AAPG Bull. 99, 2121–2154.
Yuan, G.H., Cao, Y.C., Jia, Z.Z., Gluyas, J., Yang, T., 2015b. Selective dissolution of feldspars in the presence of carbonates: the way to generate secondary pores in buried sandstones by organic $CO_2$. Mar. Petrol. Geol. 60, 105–119.
Yuan, G.H., Cao, Y.C., Schulz, H.M., Hao, F., Gluyas, J., Liu, K.Y., Yang, T., Wang, Y.Z., Xi, K.L., Li, F.L., 2019a. A review of feldspar alteration and its geological significance in sedimentary basins: from shallow aquifers to deep hydrocarbon reservoirs. Earth Sci. Rev. 191, 114–140.
Yuan, W., Liu, X.R., Fu, Y., 2019b. Chemical thermodynamics and chemical kinetics analysis of sandstone dissolution under the action of dry-wet cycles in acid and alkaline environments. Bull. Eng. Geol. Environ. 78, 793–801.
Zahid, M.A., Chunmei, D., Lin, C., Gluyas, J., Jones, S., Zhang, X.G., Munawar, M.J., Ma, C.F., 2016. Sequence stratigraphy, sedimentary facies and reservoir quality of Es4s, southern slope of Dongying Depression, Bohai Bay Basin, East China. Mar. Petrol. Geol. 77, 448–470.
Zhang, C.L., Sun, W., Gao, H., Xi, T.D., He, Q.Y., Shi, J.C., Qu, L., 2014. Quantitative calculation of sandstone porosity evolution based on thin section data: a case study from Chang 8 reservoir of Huanjiang Area, Ordos Basin. Acta Sedimentol. Sin. 32, 365–375 (in Chinese with English abstract).
Zhao, W.Z., Jia, C.Z., Jiang, L., Zhang, T., He, M.X., Zhang, F., Jiang, Z.X., Li, X.F., Wu, K. L., 2021. Fluid charging and hydrocarbon accumulation in the sweet spot, Ordos Basin, China. J. Petrol. Sci. Eng. 200, 108391.
Zhong, D.K., Zhu, X.M., Zhou, X.Y., Wang, Z.M., 2007. An approach to categories and mechanisms of SiO2 dissolution in sandstone reservoirs in the Tarim Basin. Chinese J. Geol. 42, 403–414.
Zhou, Y., Ji, Y.L., Xu, L.M., Che, S.Q., Niu, X.B., Wan, L., Zhou, Y.Q., Li, Z.C., You, Y., 2016. Controls on reservoir heterogeneity of tight sand oil reservoirs in Upper Triassic Yanchang Formation in Longdong Area, southwest Ordos Basin, China: implications for reservoir quality prediction and oil accumulation. Mar. Petrol. Geol. 78, 110–135.
Zhu, H.H., Zhong, D.K., Yao, J.L., Sun, H.T., Niu, X.B., Liang, X.W., You, Y., Li, X., 2015. Alkaline diagenesis and its effect son reservoir porosity: a case study of Upper Triassic Chang7 Member tight sands to nein Ordos Basin, NW China. Petrol. Explor. Dev. 42, 56–65 (in Chinese with English abstract).
Zou, C.N., Zhang, G.Y., Tao, S.Z., Hu, S.Y., Li, X.D., Li, J.Z., Dong, D.Z., Zhu, R.K., Yuan, X.J., Hou, L.H., 2010. Geological features, major discoveries and unconventional petroleum geology in the global petroleum exploration. Petrol. Explor. Dev. 37, 129–145.
Zou, C.N., Pan, S.Q., Horsfield, B., Yang, Z., Hao, S.Y., Liu, E.T., Zhang, L.F., 2019. Oil retention and intrasource migration in the organic-rich lacustrine chang 7 shale of the upper triassic yanchang formation, Ordos Basin, central China. AAPG Bull. 103, 2627–2663.